HAL open science

Dynamic core-periphery structure of information sharing networks in entorhinal cortex and hippocampus

Nicola Pedreschi, Christophe Bernard, Wesley Clawson, Pascale P. Quilichini, Alain Barrat, Demian Battaglia

To cite this version:

Nicola Pedreschi, Christophe Bernard, Wesley Clawson, Pascale P. Quilichini, Alain Barrat, et al.. Dynamic core-periphery structure of information sharing networks in entorhinal cortex and hippocampus. Network Neuroscience, 2020, 4 (3), pp.946-975. 10.1162/netn_a_00142 . hal-02956203

HAL Id: hal-02956203

https://amu.hal.science/hal-02956203

Submitted on 2 Oct 2020

HAL is a multi-disciplinary open access archive for the deposit and dissemination of scientific research documents, whether they are published or not. The documents may come from teaching and research institutions in France or abroad, or from public or private research centers.

L'archive ouverte pluridisciplinaire **HAL**, est destinée au dépôt et à la diffusion de documents scientifiques de niveau recherche, publiés ou non, émanant des établissements d'enseignement et de recherche français ou étrangers, des laboratoires publics ou privés.

Distributed under a Creative Commons Attribution 4.0 International License

NETWORK NEUROSCIENCE

an open access journal

Citation: Pedreschi, N., Bernard, C., Clawson, W., Quilichini, P., Barrat, A., & Battaglia, D. (2020). Dynamic core-periphery structure of information sharing networks in entorhinal cortex and hippocampus. *Network Neuroscience, 4*(3), 946–975. https://doi.org/10.1162/netn_a_00142

DOI: https://doi.org/10.1162/netn_a_00142

Supporting Information: https://doi.org/10.1162/netn_a_00142

Received: 17 January 2019
Accepted: 16 April 2020

Competing Interests: The authors have declared that no competing interests exist.

Corresponding Authors:
Alain Barrat
alain.barrat@cpt.univ-mrs.fr
Demian Battaglia
demian.battaglia@univ-amu.fr

Handling Editor:
Olaf Sporns

Copyright: © 2020
Massachusetts Institute of Technology
Published under a Creative Commons Attribution 4.0 International (CC BY 4.0) license

The MIT Press

RESEARCH

Dynamic core-periphery structure of information sharing networks in entorhinal cortex and hippocampus

Nicola Pedreschi[1,2], Christophe Bernard[2], Wesley Clawson[2], Pascale Quilichini[2], Alain Barrat[1,3], and Demian Battaglia[2]

[1]Aix-Marseille University, Université de Toulon, CNRS, CPT, Turing Center for Living Systems, Marseille, France
[2]Aix-Marseille University, Inserm, INS, Institut de Neurosciences des Systèmes, Marseille, France
[3]Tokyo Tech World Research Hub Initiative (WRHI), Institute of Innovative Research, Tokyo Institute of Technology, Japan

Keywords: Temporal networks, Information theory, Hippocampus, Entorhinal cortex, Cell assemblies, Dynamic functional connectivity

ABSTRACT

Neural computation is associated with the emergence, reconfiguration, and dissolution of cell assemblies in the context of varying oscillatory states. Here, we describe the complex spatiotemporal dynamics of cell assemblies through temporal network formalism. We use a sliding window approach to extract sequences of networks of information sharing among single units in hippocampus and entorhinal cortex during anesthesia and study how global and node-wise functional connectivity properties evolve through time and as a function of changing global brain state (theta vs. slow-wave oscillations). First, we find that information sharing networks display, at any time, a core-periphery structure in which an integrated core of more tightly functionally interconnected units links to more loosely connected network leaves. However the units participating to the core or to the periphery substantially change across time windows, with units entering and leaving the core in a smooth way. Second, we find that discrete network states can be defined on top of this continuously ongoing liquid core-periphery reorganization. Switching between network states results in a more abrupt modification of the units belonging to the core and is only loosely linked to transitions between global oscillatory states. Third, we characterize different styles of temporal connectivity that cells can exhibit within each state of the sharing network. While inhibitory cells tend to be central, we show that, otherwise, anatomical localization only poorly influences the patterns of temporal connectivity of the different cells. Furthermore, cells can change temporal connectivity style when the network changes state. Altogether, these findings reveal that the sharing of information mediated by the intrinsic dynamics of hippocampal and entorhinal cortex cell assemblies have a rich spatiotemporal structure, which could not have been identified by more conventional time- or state-averaged analyses of functional connectivity.

AUTHOR SUMMARY

It is generally thought that computations performed by local brain circuits rely on complex neural processes, associated with the flexible waxing and waning of cell assemblies, that is, an ensemble of cells firing in tight synchrony. Although cell assembly formation is inherently and unavoidably dynamical, it is still common to find studies in which essentially "static" approaches are used to characterize this process. In the present study, we adopt instead a temporal network approach. Avoiding usual time-averaging procedures, we reveal that hub neurons are not hardwired but that cells vary smoothly their degree of integration within the

assembly core. Furthermore, our temporal network framework enables the definition of alternative possible styles of "hubness." Some cells may share information with a multitude of other units but only in an intermittent manner, as "activists" in a flash mob. In contrast, some other cells may share information in a steadier manner, as resolute "lobbyists." Finally, by avoiding averages over preimposed states, we show that within each global oscillatory state rich switching dynamics can take place between a repertoire of many available network states. We thus show that the temporal network framework provides a natural and effective language to rigorously describe the rich spatiotemporal patterns of information sharing instantiated by cell assembly evolution.

INTRODUCTION

Cell assembly:
Group of cells firing repeatedly in a coordinated manner and serving as a functional entity for neuronal information processing; that is, a set of cells "working together."

Since its early definitions (Abeles, 1982; Hebb, 1949), the notion of *cell assembly*, loosely defined as a group of neurons with coordinated firing within a local or distributed circuit, has been associated with information processing. According to a widely accepted view (see, e.g., Varela, Lachaux, Rodriguez, & Martinerie, 2001), neuronal representations and, more generally, computations are constructed via the dynamic integration of the information conveyed by the spiking activity of different cells. The recruitment of a cell assembly goes thus well beyond the mere coactivation of an ensemble of cells frequently firing together. It corresponds indeed to the instantiation of an actual transient functional network allowing information to be shared between neurons and fed into novel informational constructs suitable for further processing (Buzsáki, 2010).

In this sense, it appears quite natural to describe the flexible creation, transformation, and dissolution of groups of information-exchanging neurons as a dynamic network whose nodes and edges evolve through time, reflecting the recruitment (or the dismissal) of neurons into (or out of) the integrated assembly. Nevertheless, cell assemblies at the level of neuronal microcircuits—and, particularly, in the hippocampal formation, involved in spatial navigation and episodic memory (Buzsáki & Moser, 2013)—have been most often characterized in terms of sets of nodes frequently coactivating in time (Mao, Hamzei-Sichani, Aronov, Froemke, & Yuste, 2001; Miller, Ayzenshtat, Carrillo-Reid, & Yuste, 2014) or repeatedly activating in sequences (Ikegaya et al., 2004; Malvache, Reichinnek, Villette, Haimerl, & Cossart, 2016). Such "static" catalogues of patterns of firing partially fail at highlighting that the temporally coordinated firing of nodes gives rise to a dynamics of functional links (Aertsen, Gerstein, Habib, & Palm, 1989; Bonifazi et al., 2009; Clawson et al., 2019), that is, to a *temporal network* (Holme, 2015; Holme & Saramäki, 2012; Masuda & Holme, 2017).

Temporal network:
A time series of snapshots of the instantaneous network of communication between the elements of the network.

The temporal network framework has recently emerged in order to take into account that for many systems, a static network representation is only a first approximation. Studies of temporally resolved data in communication and social networks have in particular uncovered features such as broad distributions of contact or intercontact times (burstiness) between individuals (Barabási, 2005; Cattuto et al., 2010), multiple temporal and structural scales (Darst et al., 2016; Laurent, Saramäki, & Karsai, 2015; Saramäki & Moro, 2015), and a rich array of intrinsically dynamical structures that could not be unveiled within a static network framework (Galimberti, Barrat, Bonchi, Cattuto, & Gullo, 2018; Gauvin, Panisson, & Cattuto, 2014; Kobayashi, Takaguchi, & Barrat, 2019; Kovanen, Karsai, Kaski, Kertész, & Saramäki, 2011). In the neuroscience field, emphasis has been recently put on the need to upgrade "connectomics" into "chronnectomics," to disentangle temporal variability from intersubject and intercohort differences (Calhoun, Miller, Pearlson, & Adalı, 2014; Hutchison et al., 2013).

However, a majority of dynamic network studies have so far considered large-scale brain-wide networks of interregional connectivity (Thompson, Brantefors, & Fransson, 2017) and only fewer have addressed information sharing networks at the level of microcircuits, in vitro or in silico (Orlandi, Soriano, Alvarez-Lacalle, & Teller, 2013; Poli, Pastore, & Massobrio, 2015; Stetter, Battaglia, Soriano, & Geisel, 2012), and even more rarely in vivo (Clawson et al., 2019).

Information sharing network:
A weighted network in which the weight of an edge linking two neurons represents the amount of mutual information between the activities of these neurons.

Hippocampus:
A characteristically folded neural structure belonging to the limbic system. Crucial for spatial navigation and memory, the hippocampus has various anatomical subdivisions, such as hippocampus CA1 (first zone of "cornu ammonis").

Entorhinal cortex:
An area of the brain serving as the main interface between the hippocampus and the neocortex. It is involved in functions such as memory and space-time integration and is critically affected in pathologies like Alzheimers disease.

Global oscillatory states:
Alternative modes of collective oscillation of neural activity (slower, ∼1 Hz, as in the slow oscillation state; or faster, ∼5–8 Hz), widespread across multiple brain regions, which can be detected in neural recordings.

Network states:
Discrete states of the evolution of the network in terms of its structure and rate change of connectivity.

Connectivity profile:
For each neuron, a description of its main connectivity (and connectivity variation) properties within a network state.

Here, we propose to embrace a temporal network perspective when describing dynamic information sharing within and between cell assemblies. Concretely, we analyze high-density electrophysiological recordings in the hippocampus and medial entorhinal cortex of the rat, allowing to follow in parallel the spiking activity of several tens of single units in different brain regions and layers. We focus on recordings performed during anesthesia, guaranteeing long and stable recordings of intrinsic cell assembly dynamics over several hours (Quilichini, Sirota, & Buzsáki, 2010). Indeed, even during anesthesia, the spatiotemporal complexity of firing is not suppressed but a wide repertoire of cofiring ensembles and associated information processing modes can be found (Clawson et al., 2019). Furthermore, with the used anesthesia protocol, we observe a characteristic stochastic alternation between two global brain oscillatory states, respectively dominated by slow oscillations (SO) and theta (THE) oscillations (see *Methods*). Such experimental condition is therefore particularly suitable to probe the dependence of cell assembly dynamics on the currently active global oscillatory state (Clawson et al., 2019), which is expected to be a major modulator of information processing in the hippocampus formation (Buzsáki & Moser, 2013; Klausberger et al., 2003) and cortical circuits in general (Gilbert & Sigman, 2007; Varela et al., 2001). Using a sliding window approach, we extract temporal networks of information sharing between cells, and we develop methods to investigate how their connectivity properties evolve in time.

At the level of whole network organization, we pay attention to whether connectivity structure changes continuously—as in the case of many social or communication networks (Cattuto et al., 2010; Miritello, Lara, Cebrian, & Moro, 2013; Saramäki & Moro, 2015)—or rather undergoes switching between different discrete network states—as recently observed for instance in an animal social network (Gelardi, Fagot, Barrat, & Claidière, 2019)—possibly in relation to transitions between global oscillatory states. We find that switching between *discrete network states* does spontaneously occur during anesthesia. Remarkably, we identify a multiplicity of states of connectivity between single neurons, with rich switching dynamics ongoing even in the absence of a change in the global oscillatory state. The sharing network connectivity, however, is never frozen, but keeps fluctuating within each of the network states. More specifically, at any time, the instantaneous information sharing network displays a core-periphery organization (Della Rossa, Dercole, & Piccardi, 2013; Kojaku & Masuda, 2018), in which a limited number of neurons form a tightly mutually connected core, while a majority of other neurons are more peripheral. Individual neurons through time modulate their degree of integration within the sharing network and may "float" between the core and the periphery, transiently leaving or getting engaged into the core, giving rise to what we call a *liquid core-periphery* architecture.

At the level of single nodes, the neighborhood of each neuron is constantly evolving. Most importantly, neurons that have at the time aggregated level similar static connectivities, having connections for a comparable overall amount of time, can strongly differ in their temporal connectivity profile. For instance, some neurons may form links that remain active for a limited amount of time but in an uninterrupted way. Other neurons may instead repeatedly connect and disconnect to others, sharing information in an intermittent and sporadic fashion. We thus define for each neuron its specific temporal connectivity profile, which summarizes its

Connectivity styles:
Typical classes of connectivity profiles that reoccur over the time of a recording and across all recordings.

dynamic patterns of attachment in the evolving core-periphery sharing network. We then use an unsupervised classification approach to identify *temporal connectivity style archetypes* and show that neurons can adopt different styles in different network states, possibly associated with variations of their role in information processing (see *Discussion*).

Going beyond averaged network analyses with suitable time-resolved metrics allows thus an unprecedented precision in characterizing the functional organization of information sharing. Cell assemblies are not anymore seen as rigidly defined groups of cells but as dynamic networks, restlessly exchanging flows of information between core and periphery and continuously modifying their extent and reach toward cells in different anatomical locations. In other words, the adoption of a temporal network framework makes it possible to witness and seize the inner life of cell assemblies while it unfolds and gives rise to emergent computations.

RESULTS

Information Sharing Dynamics Can Be Described as a Temporal Network

Single unit recordings of neuronal activity were acquired simultaneously from the CA1 region in the hippocampus and in the mEC (Figure 1A and Supporting Figure S1) for 16 rats under anaesthesia (18 recordings for 16 rats). Following Clawson et al. (2019), we constructed time-resolved weighted networks of functional connectivity, adopting a sliding window approach. Within each 10-s-long time window, we took connection weights (functional links) between pairs of neurons (network nodes) to be proportional to the amount of *shared information* (Kirst, Timme, & Battaglia, 2016) between their firing rates. Only links whose strength exceeded a general significance threshold were kept (see *Methods*). We then slide the time window by 1 s, in order to achieve a 90% overlap between consecutive windows. In Figure 1B, we represent the temporal network construction procedure. Based on the data segments in each of three windows centered at times t_a, t_b, and t_c, we extract an $N \times N$ matrix for each time window, where N is the number of neurons and in which the element (i, j) corresponds to the shared information between nodes i and j. Each such matrix, in network terms, is interpreted as the *adjacency matrix* of a weighted graph G of N nodes. Even if the used functional connectivity metric is in principle pseudodirected (because of the presence of a time lag between putative sender and receiver node), we found that asymmetries between reciprocal connections were very small (see *Methods*), especially for the stronger connections, and chose therefore to symmetrize the adjacency matrix for most analyses. This procedure thus maps each multichannel recording of length T seconds to a time series of T network representations, obtaining finally a temporal network of information sharing among neurons, formed by the temporal succession of these T network snapshots. Cartoon representations of the temporal network snapshots $G(t_a)$, $G(t_b)$, and $G(t_c)$ in the three highlighted time windows are shown in Figure 1C. Some actual network frames of a specific recording, together with a diagram describing emergence and disappearance of links (*edge activity plot*), can be seen in Figure 2.

On the top of Figure 1B we also present the characteristic switching between global oscillatory states observed in our recordings. Analysis of the local field potentials recorded simultaneously to single unit activity allowed identifying a spontaneous stochastic-like alternation between epochs belonging to a first SO global state (light blue color) spectrally dominated by < 1 Hz oscillations and epochs in a second THE global state, characterized by the presence of high power in a 4–8 Hz spectral band. In the following we will relate the temporal network reconfiguration dynamics to these global oscillatory state transitions.

We carried on our study by analyzing in parallel the evolution of the weighted temporal network structure and of the corresponding unweighted temporal network. To this aim we

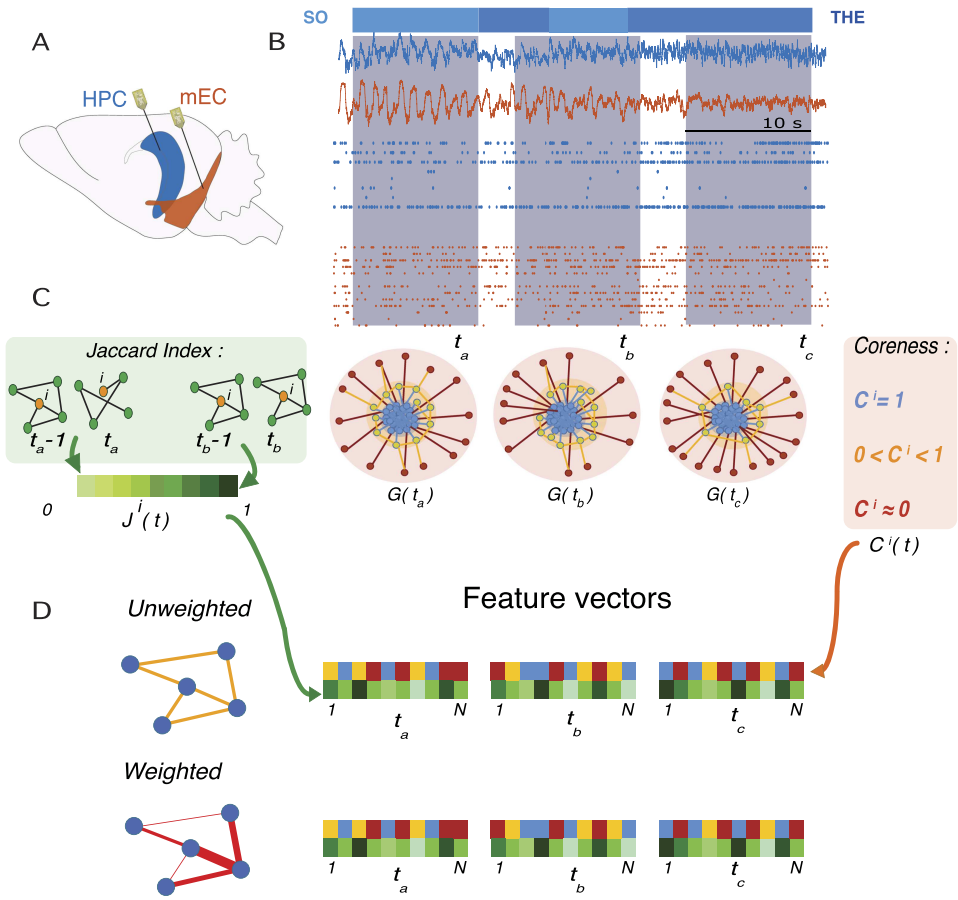

Figure 1. Recordings and feature vectors. (A) Approximate recording locations in mEC (orange) and CA1 (blue) during anesthesia. (B) An example of LFP signal recorded by the channels in CA1 and in mEC; below the LFPs are two examples of single-unit activity from the same recording. The intervals t_a, t_b, and t_c are examples of time windows in which the corresponding network time-frames are constructed. The horizontal bar above the recordings represents the global oscillation states: in light blue the *slow oscillations* and in darker blue the *theta oscillations*. (C) Illustrative sketches of the two features computed for each node at each time-frame: On the left, in the green box, we illustrate the *Jaccard index*, which quantifies the overlap between two sets. Here we consider the local Jaccard indices between the neighborhoods of each node $i \in [1, N]$ in successive time frames (e.g., $J^i(t_a)$ is the Jaccard index for node i between times $t_a - 1$ and t_a): these quantities carry information on how little or how radically the neighborhoods of i change across time, and we call them *liquidity*. The center and right panels are a schematic representation of the core-periphery organization of the network and the intuitive explanation of the *coreness* C values of the nodes: *core* (blue) nodes have high values of coreness $C \sim 1$, whereas peripheral (red) nodes have low values, $C \sim 0$; the yellow area surrounding the core is the *core-skin*, i.e., nodes whose coreness values are higher than 0 and lower than 1. When a node is *disconnected* from the rest of the network (when it has no neighbors), its coreness is exactly zero. (D) At each time frame, we obtain feature vectors of the coreness and liquidity values of all neurons $i \in [1, N]$, schematized by the two colorful vectors (yellow, blue, and red for coreness and green for liquidity). The analyses were performed both for unweighted networks, in which links are either present or absent, and for weighted networks, in which the links are characterized by a weight given by the amount of shared information between the nodes. For weighted networks, liquidity is measured by the cosine similarity instead of the Jaccard index (see *Methods*), and a weighted coreness is computed for each node.

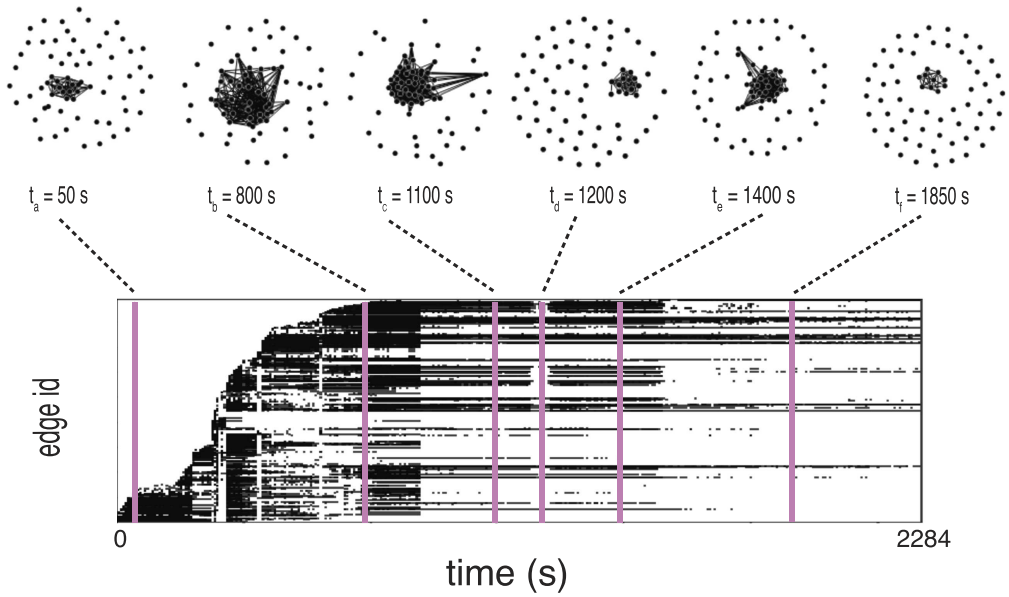

Figure 2. Temporal network visualization. Evolution of the information sharing temporal network computed for one of the recordings, represented using the visualization toolbox TACOMA (`http://tacoma.benmaier.org/about.html`). The six networks on the top plots represent six snapshots of the network's evolution at the corresponding times: Each black dot represents a neuron whose activity has been recorded at the corresponding time. The bottom panel displays the temporal network's *edge activity plot*: Each row of the plot represents the activity of one edge of the network, i.e., a black dot on a row means that the corresponding edge on the vertical axis is active (a nonzero element of the network's adjacency matrix) at the corresponding time on the horizontal axis. The edges are ordered on the vertical axis by increasing value of their *first activation time*.

defined for each time window a binarized version of the network snapshot, whose adjacency matrix is only composed of zeros and ones: The adjacency matrix element is 0 (no link is present in the unweighted network) when two nodes are not connected (i.e., MI below threshold) and it is equal to 1 when they are (MI above threshold, see *Methods*). By comparing weighted and unweighted analyses we could assess whether the network changes involve actual evolutions of the structures of the links or rather correspond only to weight modulations on a stable link structure. To quantify the dynamics of the network, we focused on two main aspects—translated into corresponding temporal network features in both weighted and unweighted versions—aimed at answering two different questions. First, are the connections of the network stable in time, or rapidly changing? Second, does the network have a clear and specific structural organization, and if so, is it persistent in time or unstable and only transient?

cosine similarity $\Theta^i(t)$:
The cosine similarity between a node i's neighborhoods at times $t-1$ and t is defined as

$$\Theta^i(t) \equiv \frac{\sum_j w_{ij}(t-1)w_{ij}(t)}{\sqrt{\sum_j w_{ij}(t-1)^2}\sqrt{\sum_j w_{ij}(t)^2}},$$

where $w_{ij}(t)$ is the weight of the link between nodes i and j at time t.

In order to answer the first question, we quantified, for each neuron i, how much its neighborhood changed between successive time windows (Gelardi et al., 2019; Miritello et al., 2013; Stehlé, Charbonnier, Picard, Cattuto, & Barrat, 2013; Valdano et al., 2015). To this aim we computed for each i and at each time t the *cosine similarity* $\Theta^i(t)$ between the neighborhoods of i (the subgraphs composed only by the edges involving i) at time $t-1$ and at time t. To analyze the unweighted temporal networks, we instead used the *Jaccard index* $J^i(t)$ between these successive neighborhoods (see side jargon boxes for precise definitions). Values of these quantities close to or equal to 1 suggest that the node has not changed neighbors in successive time windows: hence its neighborhood shows low *liquidity* (elsewhere, it would be said that the node shows high "loyalty," Valdano et al., 2015). On the contrary, values close

Jaccard index $J^i(t)$:
The local *Jaccard index* for node i at time t (Figure 1C) is defined as

$$J^i(t) \equiv \frac{|\nu^i(t-1) \cap \nu^i(t)|}{|\nu^i(t-1) \cup \nu^i(t)|},$$

where $\nu^i(t-1)$ and $\nu^i(t)$ are the neighborhoods of node i at times $t-1$ and t, respectively. $J^i(t) = 0$ when $\nu^i(t-1)$ and $\nu^i(t)$ are two disjoint sets of nodes, while $J^i(t) = 1$ when the two sets are identical.

coreness coefficient $C^i(t)$:
In a static, unweighted, undirected network, the coreness C^i of node $i \in [1, N]$ is a real number between 0 and 1, interpreted as follows: When $C^i \sim 1$ the node belongs to the *core* of the network, i.e., a set of tightly connected nodes; when $C^i \simeq 0$ the node belongs instead to the network's *periphery*, i.e., is only loosely linked to the rest of the network.

to or equal to 0 mean that the neuron has completely changed neighbors between subsequent times: Its neighborhood is highly liquid. At each time t, the set of cosine similarity values $\Theta^i(t)$, $i \in [1, N]$ and the Jaccard index values $J^i(t)$, $i \in [1, N]$ (for the unweighted case) form the time-dependent feature vectors $\mathbf{\Theta}(t)$ and $\mathbf{J}(t)$, each of dimension N (Figure 1D).

In order to answer the second question and probe for the presence of specific network architectures, we considered the *core-periphery* organization of the graph. This way of characterizing the information sharing network snapshots was suggested to us by the visual inspection of their spatial embeddings, some of which are represented in Figure 2. We thus computed the *coreness coefficient* $C^i(t)$ of each node i in each snapshot t, using the definition of coreness introduced by Della Rossa et al. (2013), which quantifies how peripheral or centrally integrated each node is in the network (see *Methods* and side jargon box). We thus obtain a time-dependent vector $\mathbf{C}(t)$ of dimension N by computing at each time t the coreness $C^i(t)$ for each node $i \in [1, N]$ in the network of time window t. The computation of coreness coefficient can also be performed for weighted networks (Della Rossa et al., 2013), yielding a time series of vectors $\{\mathbf{C}_w(t) | t \in [0, T]\}$ (with $\mathbf{C}_w(t) = \{C^i_w(t), i \in [1, N]\}$).

Information Sharing Networks Have a Soft Core-Periphery Architecture

In order to investigate the core-periphery organization of the information sharing networks, we looked at the distributions of the instantaneous coreness values $C^i(t)$ over all neurons and time frames. A weighted coreness distribution from a representative recording is shown in Figure 3A (see Supporting Figure S2 for equivalent unweighted coreness analyses). Figure 3B moreover displays instantaneous distributions of the weighted coreness, for the same recording and for several time frames. We found that, within each time frame, a majority of neurons had low coreness values, that is, they were peripheral nodes in the instantaneous sharing network (red color in the cartoons of Figure 3A), while fewer neurons had high coreness values. Interestingly, in most recordings there was not a sharp separation between core and periphery. On the contrary, we generically observed the presence of a smooth distribution spanning all possible coreness values. The transition between core and periphery was thus smooth, without gaps but with neurons displaying gradually less tight links with the core, without yet being fully peripheral. We note that such smooth distributions are actually encountered in many systems (Della Rossa et al., 2013), a strict distinction between a very central core and a very loose periphery being only a schematic idealized vision and real networks displaying typically hierarchies of scales and local connectivities.

We moreover compared this empirical soft core-periphery structure with one of three different *null models*, that is, randomized versions of the data that preserve, at each time slice, increasing amounts of the empirical data structure (see *Methods*): The first null model preserves only the numbers of nodes and edges at each time step; the second preserves in addition the degree of each node at each time; the third shuffles randomly link weights over an otherwise fully preserved connectivity structure. As shown by Supporting Figure S3, the distributions of node coreness were strongly modified for all three null models, with substantially reduced or suppressed counts of nodes with large coreness values with respect to the empirical distributions. This means that null models do not display the core-periphery structure found in actual data, in particular no core is found in these null models. Therefore, the empirically found core-periphery structure is not due to simple local properties (which are preserved in some of the randomized versions) but encodes nontrivial higher order correlations.

The analyses of Figure 3A and 3B indicate that at any time frame the sharing network has a soft core-periphery architecture, but they do not inform us about how individual neurons evolve in time within this architecture. In order to follow dynamic changes in the coreness of individual neurons, we studied the time evolution of this feature for each neuron of each recording. In Figure 3C we plot the coreness $C_w^i(t)$ versus time, for each node $i \in [1, N]$ of a representative recording. The two highlighted lines in the figure represent the coreness evolution of two particular nodes. In light green, we show the instantaneous coreness of the node with maximum average coreness $\langle C_w^i(t) \rangle_T$ (averaged over the recording length T). The figure shows clearly that this neuron's instantaneous coreness is always large: The corresponding neuron is persistently part of the network's core throughout the whole recording. This contrasts with the purple line, which displays the instantaneous coreness of the neuron with largest coreness standard deviation ($\sigma(\langle C_w^i(t) \rangle_T)$): The curve fluctuates from high to low coreness values, indicating that the corresponding neuron switches several times between central core positions in the network and more peripheral ones. The contrast between these two behaviors is highlighted in the cartoon at the bottom of Figure 3C. Note that even in the randomized versions of the data, coreness values of a given node fluctuate (see Supporting Figure S3) as, in particular, disconnected nodes have zero coreness. The range of fluctuations is however reduced with respect to the original data, since the maximum coreness values are themselves much smaller.

The continuous range of observed instantaneous coreness values and the fluctuations in individual coreness values indicate that the set of most central neurons changes in time. We thus examined whether some regions were contributing more than others to this core. To this aim, we define the core, at each time frame, as the set of neurons whose instantaneous coreness lies above the 95th percentile of the distribution (in histograms such as those in Figure 3B). In Figure 3D we then plot the *core filling factors* of the CA1 and mEC layers (top and center plots, respectively). We define the core filling factor of each region as the percentage of the overall number of neurons of the recording located in that region that belong to the core. We plot the time evolution core filling factors separately for neurons located in different hippocampal CA1 layers (light and dark blue lines, top panel) and for neurons in different medial entorhinal cortex (mEC) layers (red, orange, and yellow lines, center panel). The figure illustrates that the core filling factors vary substantially through time. In the example shown here (corresponding to the same recording as in Figure 3C), the core filling factor of CA1 stratum pyramidale (SP) neurons belonging to the core increases from $\sim 2\%$ to near 7% during the recording.

The results of Figure 3D indicate that the core is not restricted to neurons belonging to a specific region, but is generally composed of both neurons belonging to EC and neurons belonging to CA1. We remind indeed that our networks are networks of functional connectivity and do not have to reflect necessarily the underlying anatomical connectivity (for which it would be unlikely that our recordings pick up monosynaptically connected cells between different regions). However, the participation of CA1 and EC neurons to the core is changing through time and, as a result, the core is sometimes "more on the EC side" or "more on the CA1 side" (see lower cartoons in Figure 3D). To visualize the relative fractions of core neurons belonging to the two different regions, we computed and show in the bottom panel of Figure 3D the normalized *core filling regional fractions*: The fraction of core nodes belonging either to EC (orange) or CA1 (blue)—the sum of these two fractions adding up to 1. The orange and blue bands change thickness through time, reflecting in this recording a progressive shift from a low to a higher involvement of CA1 neurons in the core. This variation of the multiregional core composition may reflect changes in the way the different regions control information integrative processes (see *Discussion*).

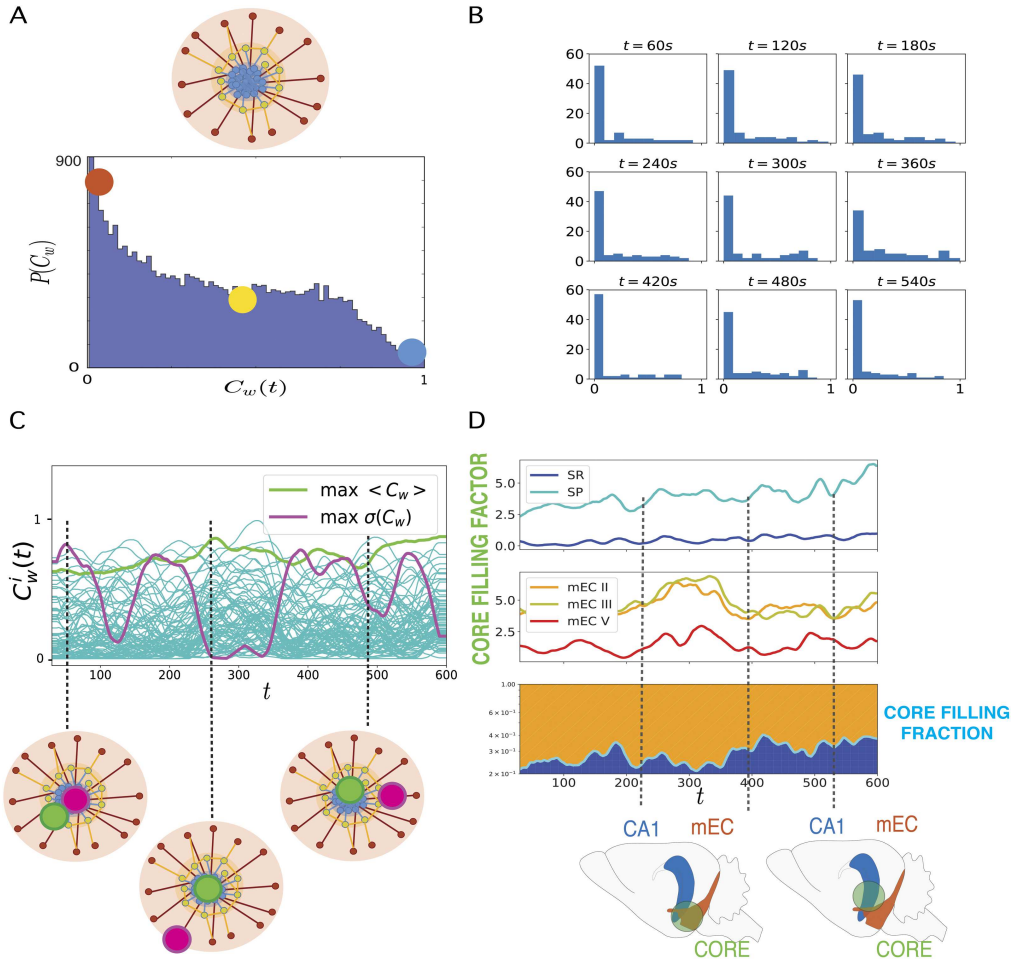

Figure 3. Dynamic core-periphery structure. (A) Top: Cartoon representing the *core-periphery* organization of the network with *core* nodes colored in blue and *peripheral* nodes in red. Bottom: Histogram of the values of the instantaneous weighted coreness $C^i(t)$ of each neuron at each time of a recording: The most frequent values of $C_w^i(t)$ are close to 0 (red dot), hence coreness values typical of *peripheral* nodes, whereas coreness values of core nodes, $C^i(t) \sim 1$ are rare (blue dot). (B) Histograms of instantaneous weighted coreness values of the neurons in several individual time-frames (every 60 s). The different histograms show that the picture of a majority of neurons with low coreness value and few neurons with high coreness hold at all times. The core-periphery organization of the information sharing network is thus persistent in time. (C) Plot of the temporal evolution of the weighted coreness $C_w^i(t)$ of each node i in a specific recording: The green line highlights the evolution of the coreness of the node with highest average coreness $\langle C_w(t) \rangle_{max}$ (time average over the whole recording); the purple line corresponds to the node whose coreness fluctuates the most (node of maximum variance of $C_w^i(t)$). We show below this plot a cartoon of the core-periphery organization of the network, where we illustrate how the former node steadily belongs to the core, while the latter node evolves several times from the core to the periphery and back. (D) Plots of the *core filling factor* (top and center panels) and of the *core filling fraction* (bottom) of the different layers of *hippocampus* (HPC) and medial *entorhinal cortex* (mEC). The core filling factor of each layer is the percentage of nodes of each layer that are located in the core (nodes above the 95th percentile of coreness values). In the bottom panel, the green line represents the separation between the fraction of core nodes located either in the mEC layers (orange) or in the HPC (blue): the *core filling fraction*. The cartoon below the core filling fraction plot illustrates how the neurons that belong to the core at different times can be located in different anatomical structures.

Network States

As previously mentioned and summarized in Figure 1C, for each recording and each time window t, we computed for each neuron $i \in [1, N]$ several temporal network properties, tracking notably the "liquidity" of its neighborhood (Jaccard index and cosine similarity) and its position within the core-periphery architecture (weighted and unweighted instantaneous coreness values). To investigate how these properties change dynamically at the global network level, we computed for each of these four quantities the correlation between their values at different times, obtaining four correlation matrices of size $T \times T$. For instance, the element (t, t') of the unweighted liquidity correlation matrix is given by the Pearson correlation between the N values of the Jaccard coefficient computed at t $\{J^i(t),\ i \in [1, N]\}$ and the N values computed at t' $\{J^i(t'),\ i \in [1, N]\}$ (see *Methods* for definition). In Figure 4A, we show these four correlation matrices for a representative recording, two for the unweighted features (above, Jaccard index and unweighted coreness), and two for the weighted ones (below, cosine similarity and weighted coreness).

The block-wise structure of these correlation matrices suggests the existence of epochs in time where neurons' feature values are strongly correlated (red blocks on the diagonal). In the case of Figure 4A, mostly diagonal blocks are observed, with low correlation values outside the blocks, meaning that the network configurations are similar during each epoch but very different in different epochs. In other cases, we sometimes observe as well off-diagonal blocks, indicating that the network might return to a configuration close to one previously observed (we show an example of this behavior in Supporting Figure S4, as well as an example in which only one epoch is observed). Each block on the diagonal (epoch in which the node properties are strongly correlated) can be interpreted as a network connectivity configuration associated with specific liquidity and coreness assignments of the various neurons. We call these configurations *network states*.

To quantitatively extract such discrete network states, we use the time series of the feature vectors $\mathbf{\Theta}(t)$, $\mathbf{J}(t)$, $\mathbf{C}_w(t)$, and $\mathbf{C}(t)$. We concatenate these vectors two by two at each time, obtaining two $2N$-dimensional feature vectors: The first one contains at each time the values of the unweighted liquidity and coreness of all nodes ($\{\mathbf{J}(t), \mathbf{C}(t)\}$), and the second one contains the corresponding weighted values ($\{\mathbf{\Theta}(t), \mathbf{C}_w(t)\}$). We then perform in each case (weighted and unweighted) an unsupervised clustering of these T $2N$-dimensional feature vectors. As a result of this clustering procedure, as shown in Figure 4A, we obtain a sequence of states (temporal clusters of the feature vectors) that the network finds itself in at different times (yellow state spectrum for the unweighted case, red for the weighted case).

We also observe that these states are not a mere artificial construction. Our procedure would segment the temporal network into states even if discretely separated clusters did not exist, but we explicitly checked that, for all recordings but two, clustering was meaningful: Supporting Figure S5A shows indeed that clustering quality was in a large majority of cases well above chance level (see *Methods*). Furthermore, when repeating the same analysis on the three null model, as shown in Supporting Figure S6A, we found that the quality of the clustering performed on the features vectors to extract the network states decreased sensibly for the randomized networks (Supporting Figure S6B). This shows that empirical temporal networks display a nonrandom level of structuration into connectivity states.

We compared the network states spectra found for the weighted and unweighted case by computing the mutual information between the two sequences of states for each recording, normalized by the largest entropy among the entropies of the two distinct sequences. Such

relative mutual information is bounded in the unit interval and quantifies the fraction of information that a state sequence carries about the other (reaching the unit value when the two state sequences are identical, and being zero if the two sequences are statistically independent). We compute this quantity for each recording and display the distribution of values obtained as a light green boxplot on the left of Figure 4B. This boxplot shows that the mutual information values between the weighted and unweighted network states sequences of a recording are concentrated around a median approaching 0.8. Therefore, the spectra of network states extracted by the weighted and unweighted analyses are generally matching well, indicating the robustness of their extraction procedure. Most importantly, the high degree of matching between weighted and unweighted analyses confirms that network state changes correspond to actual connectivity reorganizations (as revealed by unweighted analyses) and not just to weight modulations on top of a fixed connectivity.

One may also wonder whether network state changes really depend on changes of local connectivity properties (as we implicitly assumed with our use of node-specific features) or can be already explained by variations of global network properties. We therefore considered as well the time evolution of several *global* features (see Supporting Figure S7A): the node-averaged cosine similarity (Jaccard index in the unweighted case); the node averaged coreness; the sum over all weights of all edges (number of edges in the unweighted case). We then extracted network states based now on these global features (see *Methods*) and compared the resulting state spectra with the original ones. Computing the amount of mutual information between spectra based on global and local features, we found that some degree of correlation exists, not surprisingly since the numbers of links and nodes themselves fluctuate in time, in a way preserved by null models and thus contributing to state switching dynamics. However, as shown by Supporting Figure S7B, for both weighed and unweighted state extraction analyses, the relative mutual information between global and local features-based states is of the order of only $\sim$40%. Furthermore, the mutual information between weighed and unweighted global features-based states drops to $\sim$50%, while it approached $\sim$80% for local features-based states. Together, these reduced values indicate that the consideration of local features genuinely provides additional information on top of global features fluctuations and that this information is useful to determine more consistent states.

As previously discussed, the system undergoes switching between two possible global brain states during the anesthesia recordings: These global states are associated with different oscillatory patterns, dominated by either theta (THE) or slow (SO) oscillations. We studied the relation between changes in the network state and global oscillatory state switching. To this aim, we computed the normalized mutual information between network state sequences (weighted or unweighted) and global state sequences. The distributions of the values obtained are shown as boxplots on the right of Figure 4B, for both weighted (red) and unweighted (yellow) network state sequences. In both cases, we detect positive, although low, values of the relative mutual information with global oscillatory states, with a median value close to $\sim$ 0.3. This indicates that some coordination between global oscillatory state and network state switching exists but that oscillatory state switching does not well explain network state switching. A very simple reason for this poor correlation is that, while there are just two main global oscillatory states (see, however, *Discussion*), the number of network states is not a priori limited. In fact, the statistics of the number of network states in the different recordings, shown in Figure 4C, indicate that in many recordings we could extract at least three network states and sometimes up to seven. Therefore, network state switching can occur within each oscillatory global state.

Nevertheless, it is possible that each given network state would tend to occur mostly within one specific global oscillatory state. To check whether this is the case, we computed for each

network state the fraction of times that this state occurred during THE or SO epochs. We show in Figure 4D the histograms of these time fractions, measured over the set of all network states. The light blue histogram corresponds to the fractions of time a network state manifested itself during the THE state (the dark blue histogram gives the same information but for the SO state). Both histograms are markedly bimodal, indicating that a majority of states occur during either the THE or the SO states, but not in both. In other words, network states are to a large degree oscillatory state specific. Therefore, the global oscillatory states do not fully determine the observed coreness and liquidity configurations (there may be several network states for each of the oscillatory states), but most network states can be observed only during one specific global oscillatory state and not during the other.

Connectivity Profiles and Styles

To refine our analysis, we now investigate and characterize the temporal network properties at the level of single neurons within each of the detected network states. In order to do so, we computed, for each node and in each state, a set of dynamical features averaged over all time frames assigned to the specifically considered state. We focus here on the weighted features, since the weighted and unweighted analyses provide similar results. The state-specific *connectivity profile* of a given neuron i in a given state included first the following:

- its state-averaged weighted coreness value;
- its state-averaged cosine similarity value.

Note that analogous time-resolved features were already used for network state extraction, but that we consider here state-averaged values. We also computed four additional network state-specific features, defined as follows for each node $i \in [1, N]$ in a state h spanning the set of times T^h (see explanatory cartoons in Figure 5A):

- the state-averaged strength $\langle s^i(t)\rangle_{t\in T^h} \equiv \langle \sum_j w_{ij}(t)\rangle_{t\in T^h}$, hence the state-averaged total instantaneous weight of the connections of i;
- the activation number n_a^i, the number of times that the strength of node i changes from 0 to a nonzero value within the state, hence it gives the number of time that i changes its connectivity from being isolated to being connected to at least one other neuron;
- the total connectivity time τ^i, the number of time frames within T_h in which i is connected to at least one other neuron;
- the Fano factor $\Phi^i \equiv \frac{\sigma(\langle \Delta t^i\rangle_h)}{\langle \Delta t^i\rangle_h}$; each of the n_a^i periods in which i is connected to at least one other neuron has a certain duration Δt^i (the sum of these durations is τ^i), and Φ^i, the ratio of the variance and the average of the different connectivity durations of i over the state h, quantifies whether these durations are of similar value or are very diverse.

Each neuron's temporal properties within a given state are thus summarized by the values of these overall six features, which define the neuron's state-specific connectivity profile as a six-dimensional vector. Normalizing all the features to have values between 0 and 1, connectivity profiles can be visually represented as radar plots (Figure 5B) in which the value of each feature is plotted on the corresponding radial axis.

After computing the connectivity profile of each node, in each network state and in each recording, we performed an unsupervised clustering (using K-means clustering) over all these six-dimensional connectivity profiles in order to identify categories of these profiles, which

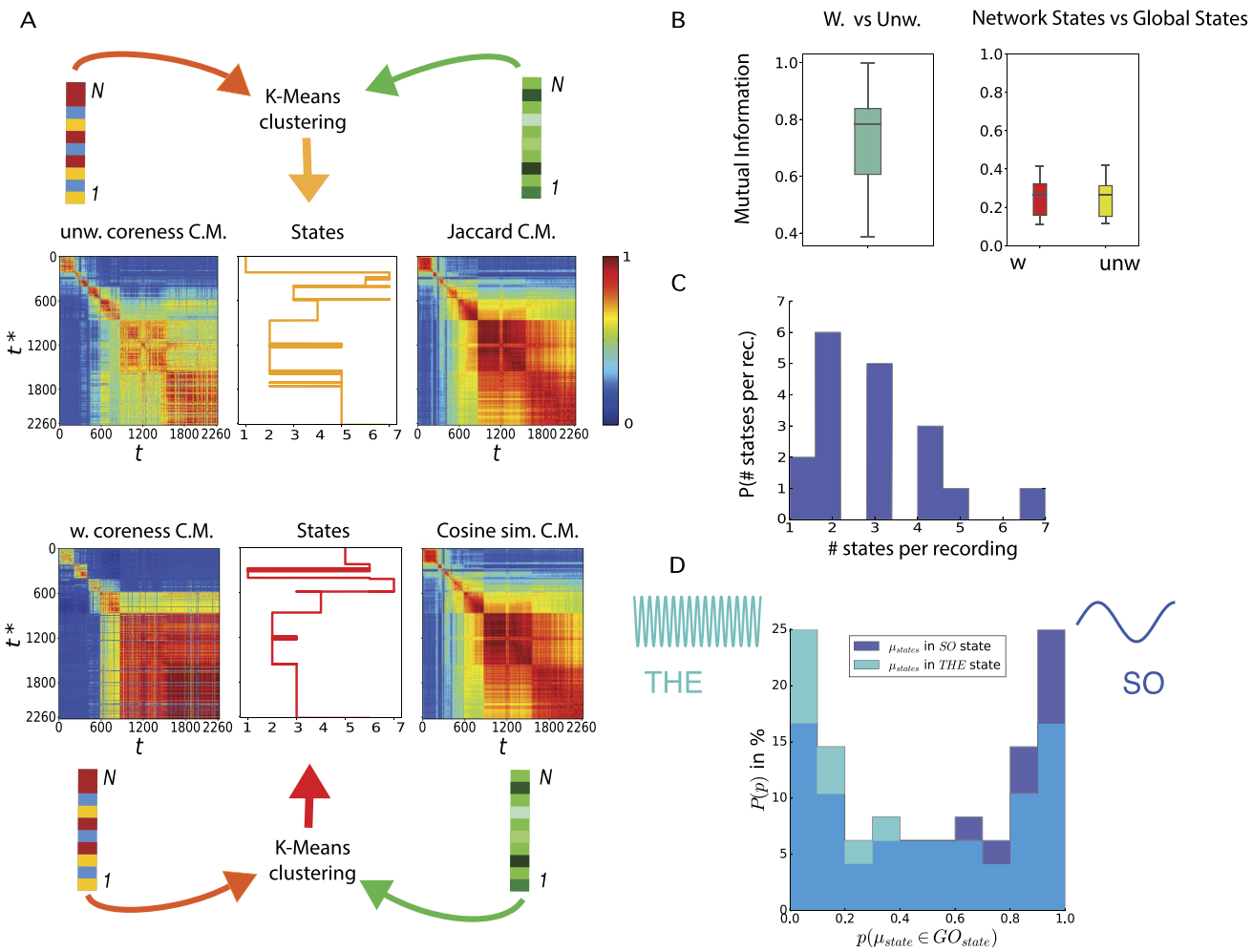

Figure 4. Liquidity and coreness network states. (A) For each recording, the feature vectors of liquidity and coreness described in Figure 1D are combined at each time, obtaining time-dependent vectors of dimension $2N$: $\{\mathbf{J}(t), \mathbf{C}(t)\}$ in the unweighted case, $\{\mathbf{\Theta}(t), \mathbf{C}_w(t)\}$ for the weighted case. K-means clustering of these vectors yields for each recording a sequence of *network states* visited by the network (center panels). We show on both sides of the network state sequences the correlation matrices (C.M.) of the various feature vectors (unweighted coreness and Jaccard, weighted coreness and cosine similarity): Each element (t, t^*) of a matrix is the Pearson correlation coefficient between the corresponding feature vectors computed at times t and t^*. For instance, the cosine similarity C.M. has as element (t, t^*) the Pearson correlation between the list of values of the cosine similarity (weighted liquidity) of nodes at times t and t^*, $\{\Theta^i(t), i = 1, \ldots, N\}$ and $\{\Theta^i(t^*), i = 1, \ldots N\}$. (B) Left panel: Distribution of the values of the mutual information between the weighted and unweighted network states spectra of all recordings: The mutual information between the two spectra is high, showing that the two spectra are highly correlated for all recordings. Right panel: Distribution of the values of mutual information between the weighted network states spectrum and the global oscillating states spectrum (red boxplot) for all recordings (yellow boxplot: same for the unweighted network states spectra). (C) Statistics of the number of network states in the different recordings. In many recordings this number is larger than 2, and it can reach values as large as 7. (D) Histograms showing the percentage of *states* having probability p to occur during a specific *global oscillation state*, *slow* (blue) or *theta* (light blue). Both histograms are bi-modal, hence the majority of *states* are strongly *global-state*-specific; the blue histogram shows an abundance of states ($\sim$ 23%) most likely to occur during the *slow* global oscillations.

we call *connectivity styles*. With this approach we uncovered the existence of four general connectivity styles that a neuron can manifest within a network state:

- *Core style (or "streamers")*, a class of nodes of high average coreness, average strength, average cosine similarity, total connectivity time, and low activation number n_a and Fano

factor Φ: overall, a class of rather central neurons with numerous stable connections that are persistently connected within a state (blue representative polygon in Figure 5B). A behavior similar to that of a speaker of an assembly, continuously conveying information to the same, and many, people: a *"streamer"* of information;

- *Peripheral style (or "callers")*, nodes with high activation number and total connectivity time but low strength, Fano factor, and coreness: a class of peripheral nodes that are periodically connected in numerous events of similar connectivity durations and low weights within a state, whose connections are neither completely liquid nor completely stable (red representative polygon in Figure 5B). A behavior similar to a customer or guest regularly making short calls to trusted core members to be updated on the latest news: aka, a "*caller*."
- *Bursty* and *regular core-skin style (or "freelancer helpers" and "staff helpers")*, two classes of connectivity profiles both characterized by nodes with intermediate coreness and strength and high values of cosine similarity and total connectivity time, whose difference lies in the values of the Fano factor Φ: the former (yellow representative polygon in Figure 5B) displaying high values of Φ can therefore be interpreted as a class of nodes that have stable connections, that are active for a long time yet with highly varying connectivity times; the latter (purple representative polygon in Figure 5B) is characterized instead by low values of the Fano factor, hence the connectivity durations of these nodes do not fluctuate much. The behaviors of these neurons can be assimilated to the one of external experts assisting core staff in a company, with either regular work schedules (the regular core-skin neurons could then be seen as *"staff helpers"*) or sporadically and irregularly (the bursty core-skin neurons could then be seen as *"freelancer helpers"*).

Note that we also identified (and subsequently discarded) an additional "junk" cluster with relatively fewer elements (9.7% of the total number of connectivity profiles computed for all neurons in all recordings) and small values of all features. We thus removed these cases, as usual in unsupervised clustering applications (Forsyth, 2018), to better discriminate the remaining "interesting" classes listed above.

Overall each connectivity profile (one for each neuron in each possible network state in the associated recording) was categorized as belonging to one of the above connectivity styles, according to the output cluster label assigned by the unsupervised clustering algorithm. However, a substantial diversity of connectivity profiles subsists within each of the clusters. We therefore considered as well a soft classification scheme, which quantifies the degree of relation of each individual connectivity profile with the tendencies identified by each of the different connectivity style clusters. Concretely, we trained a machine learning classifier to receive as input a connectivity profile and predict the connectivity style assigned to it by this unsupervised clustering. In this way, after training, the classifier assigned to each connectivity profile a four-dimensional vector whose elements represented the probabilities of belonging to any one of the four possible connectivity styles (see *Methods* for details). In Figure 5C, each connectivity profile is represented as a dot with as coordinates the soft classification labels produced by the classifier, that is, the probabilities that each given connectivity profile belongs to the periphery, core-skin (summing the probabilities for the bursty and regular subtypes), or core connectivity styles. This plot reveals, on the one hand, the existence of a gap between core (blue) and periphery (red) connectivity profiles: In other words, connectivity profiles that are likely to be classified as of the "streamer" type are very unlikely to be classified as being of the "caller" type, stressing the radical difference between these two connectivity styles. On the other hand, both the core and the periphery connectivity styles display some mixing with the core-skin style, as made clear by the almost continuous paths of connectivity profiles

from the core (blue) to the core-skin (yellow) and from the core-skin to the periphery (red). This means that there is a continuum spectrum of connectivity profiles interpolating between "streamers" and "helpers" on one side and "helpers" and "callers" on the other. The polygons shown in Figure 5B are on the contrary *archetypal* (in the sense introduced by Battaglia, Karagiannis, Gallopin, Gutch, and Cauli [2013]). These archetype profiles manifest in an extreme manner the tendencies inherent to their connectivity style. This is reflected by the fact that they lie at the vertices of the bounded soft membership space represented in Figure 5C. They display thus strong similarity to just one connectivity style, which they epitomize even better than the centroids of the associated connectivity style cluster, having near zero chance of being misclassified (cluster centroids are shown for comparison in Supporting Figure S5B).

We finally checked whether the different connectivity styles were adopted more or less frequently by neurons in specific anatomical locations or of specific types (excitatory or inhibitory). In Figure 5D, we plot the number of connectivity profiles assigned to each style (colors as in Figure 5B), separating them by anatomical layer and by brain region. However, since we recorded unequal numbers of cells in the different layers (see Supporting Figure S1), we also accounted for the different numbers of cells and recordings per layer and estimated chance-level expectations for the connectivity style counts in each layer: this allowed us to detect significant over- or underrepresentation of certain styles at different locations. The numbers of "streamers" (core), "staff helpers" (regular core-skin), and "callers" (periphery) profiles were compatible with chance levels at all the recorded locations. We only detected overrepresentations (green upward triangles) of "freelancer helpers" (bursty core-skin) in stratum radiatum (SR) of CA1 and Layer II of medial entorhinal cortex, and an underrepresentation (red downward triangle) of this style in Layer III of medial entorhinal cortex (see *Discussion* for possible interpretations). These moderate deviations from chance levels suggest that the connectivity styles adopted by different neurons (and thus their centrality in the core-periphery architecture of information sharing networks) are only poorly affected by their anatomical location in the hippocampal formation circuit, in apparent contrast with the widespread belief that the "hubness" of neurons should be strongly determined by structural and developmental factors (Cossart, 2014).

We found however a stronger interrelation between cell type and connectivity styles (Figure 5D, bottom). We still found representatives of any of the connectivity styles among both excitatory and inhibitory neurons. However we found that the fraction of inhibitory (resp., excitatory) neurons among the core neurons was significantly above (resp., below) chance level. Conversely, the fraction of inhibitory (resp., excitatory) neurons among the peripheral neurons was significantly below (resp., above) chance level (see *Discussion*).

Connectivity Profiles Are Network State–Dependent and Not Only Node-Dependent

We have computed connectivity profiles per neuron *and* per network state, in order to enable the detection of a possible network state dependency of the temporal properties of the neurons' connectivity. However, the state specificity of this computation does not prevent a priori a neuron to always assume the same connectivity profile across all possible network states in which it participates. It is thus an open question whether connectivity profiles are only node-dependent (for a given neuron, the same in every state) or, more generally, state-dependent (for a given neuron, possibly different across different network states).

To answer this question, we checked whether network state transitions are associated with connectivity style modifications at the level of individual neurons. We found that changes in the connectivity style of a neuron upon a change of state are the norm rather than the exception. We computed for every neuron the index η, quantifying the diversity of connectivity styles that

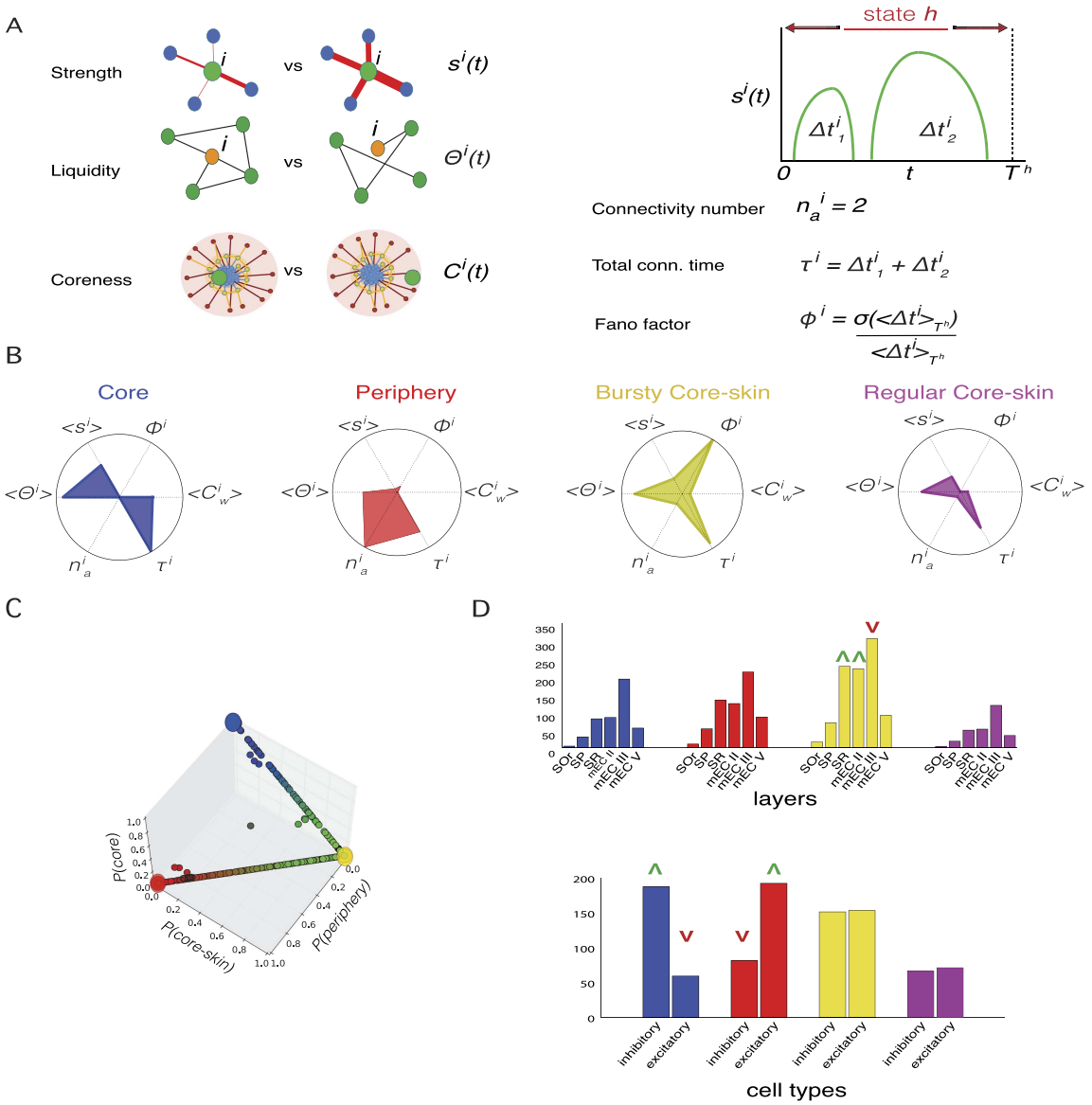

Figure 5. Connectivity profiles. (A) Cartoons illustrating the features: The *strength* $s_i(t)$ of a node i at time t measures the global importance of node i's connections (the cartoon shows a comparison of low vs. high values of $s^i(t)$); its liquidity, hence the cosine similarity (Jaccard index in the unweighted case) between successive neighborhoods (the cartoon illustrates a change between the neighborhood of i at successive times); its coreness; the connectivity number n_a^i and total connectivity time τ^i of node i in a state: τ^i represents the number of time frames in which neuron i is connected to at least one other neuron, and n_a^i is the number of times that i switches from being disconnected to being connected to at least one other neuron; the Fano factor quantifies the fluctuations of the durations of the n_a^i periods in which i is connected. (B) The connectivity profile of each neuron i in a state h is a 6-dimensional vector whose components are its *state-averaged* features: average coreness $\langle C_w^i \rangle_h$, average liquidity $\langle \Theta^i \rangle_h$, average strength $\langle s^i \rangle_h$, connectivity number n_a^i, total connectivity time τ^i, Fano factor Φ^i. Clustering of all the connectivity profiles yields four *connectivity styles* that we represent here as radar plots. We identify four main styles: core (blue), periphery (red), bursty core-skin (yellow), and regular core-skin (magenta), with different distinctive values of the different features composing the connectivity profile. Shown here are radar plots for the connectivity profile of archetypal cells in each of the connectivity styles (see *Results* for details). (C) 3D plot of the connectivity styles space: The three axes are the probabilities of the connectivity profile of a node in a network state to belong to the periphery, core-skin, or core, respectively. (D) Histograms of the layer location (top plot) of the neurons exhibiting each connectivity style (identified by the same color as panel B), and histograms of cell type (inhibitory and excitatory, bottom plot) populations per connectivity style. A green upward arrow means that the connectivity style of the corresponding color is statistically overrepresented in the corresponding layer or cell type, whereas a red downward arrow means that the connectivity style is underrepresented in that layer or cell type.

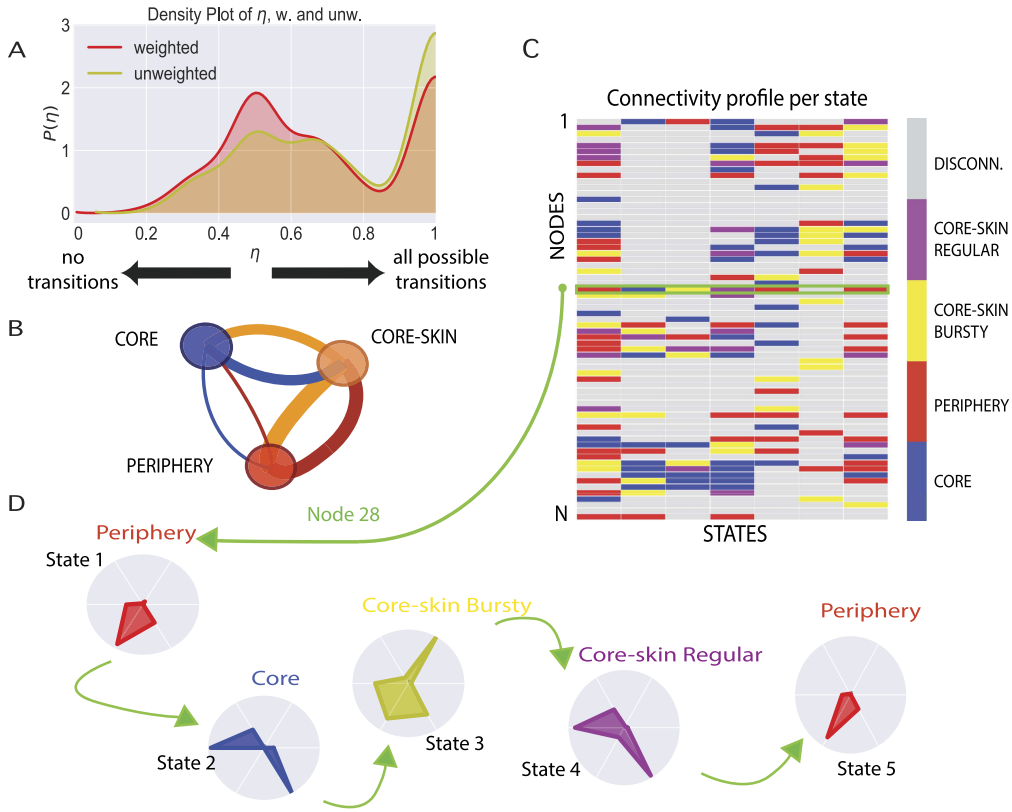

Figure 6. Network state specificity of connectivity profiles. (A) Histogram of the connectivity-style-switching probability η of nodes, in the weighted (red) and unweighted (yellow) cases, computed for each neuron in each recording. η is defined (see *Methods*) as the ratio between the number of transitions between different connectivity styles in subsequent states of a neuron during the whole recording and the maximum value between the total number of connectivity styles and number of network states observed in the recording. (B) Visualization as a weighted, directed graph of the cross–network state connectivity style transition matrix. The color of an edge corresponds to the color of the node from which it emanates. The width of an edge from connectivity style A to connectivity style B is proportional to the probability of a neuron to switch from a connectivity profile of connectivity style A in a state to a profile of connectivity style B in the next state. (C) Matrix representation of the changes in connectivity styles of the neurons when the network changes state. Each element (s, n) of the matrix is colored according to the connectivity style to which node n's connectivity profile belongs in state s. (D) Connectivity profile transitions of node $n = 28$, whose evolution is characterized by transitions between profiles belonging to different styles, highlighting how a given node can display radically different dynamical behaviors in different states.

a neuron assumes across the different network state transitions occurring during a recording. Such an index is bounded in the range $0 \leq \eta \leq 1$ and assumes the null value if the neuron always remains in the same connectivity style (no style transitions); it takes the unit value if the neuron changes connectivity style every time that a network state transition occurs, and it assumes intermediate values if style transitions occur for some of the network state transitions but not for all (see *Methods*). The distribution of the observed values of this η index is shown in Figure 6A. This distribution is bimodal, with a first peak occurring around $\eta \sim 0.5$ and a second at $\eta \sim 1$ (computed according to either unweighted or weighed network state transitions). This means that almost no neuron was associated with a network state-independent, fixed connectivity style. On the contrary, a large number of neurons changed connectivity style in

at least roughly half of the network state transitions (first mode of the distribution), and many changed style at almost each state transition (second mode of the distribution of η).

Figure 6B is a graph representation of the transition matrix between connectivity styles, computed over all the observed connectivity style transitions. We plot here a weighted, directed graph, in which the two connectivity styles "regular" and "bursty core-skin" have been merged for simplicity into a single category. The width of each colored edge corresponds to the value of the transition rate from the class of the same color. The transition rate is defined as the probability that a node characterized by one of the three connectivity styles in one network state switches to one of the other two connectivity styles in the successive network state. Consistent with Figure 5C, we find that edges of large weight connect the core-skin to the periphery and to the core in both directions: high transition rates are found between these styles. The edges connecting core and periphery are sensibly smaller. We can thus conclude that it is largely more likely that neurons of a *core* connectivity profile switch to a *core-skin* profile in the following network state than to a *peripheral* profile, and vice versa: Direct transitions between core profiles and periphery profiles are not very likely to occur, although they are not impossible. More complete transition graphs and tables (including as well the core-skin class separation into "bursty" and "regular," and the "junk" classes) are shown in Supporting Figure S8. Individual neurons can thus float through the core-periphery architecture, descending from core towards periphery and ascending back into the core, via crossing the core-skin styles.

The overall behavior of neurons' switching styles between states is illustrated in Figures 6C and 6D for a specific recording. The former is a matrix whose element (i, s) has the color of the connectivity style exhibited by node i in state s. In this plot we highlight the row corresponding to the state-wise evolution of a specific selected node, whose successive connectivity profiles in the successive network state are shown in Figure 6D.

Connectivity Profiles Only Poorly Depend on Firing Rate

In our recordings we observed a diversity of firing rates between different single units. While the median firing rate was close to ~ 1 Hz, some neurons had, at specific moments, high rates approaching 40 Hz, despite the anesthesia conditions. Importantly, firing rates were also changing across the different network states. To check whether variations of temporal connectivity features compiled in the state-specific connectivity profiles of different neurons could simply be explained by these firing rate variations, we constructed scatterplots of state-specific coreness, liquidity, strength, number of activations, Fano factors, and total time of activation for the different neurons against their firing rate, averaged over the corresponding state. These scatterplots are shown in Supporting Figure S5C.

The degree of correlation between firing rate and connectivity features was at best mild. Cells with larger than median firing rate tended to have slightly less liquid neighborhoods on average, but the range of variation was broad and largely overlapping with the one of liquidity values for lower firing rate neurons. Other features, such as total time of activation, displayed an even weaker dependence on firing rate, while some others, such as the connectivity number, tended to be inversely correlated with firing, but, once again, in a rather weak manner (the correlation coefficient is $\rho = -0.14$).

Overall, the analyses of Supporting Figure S5C indicate that the structure of information sharing networks is shaped by the coordination of firing between units more than by the firing rates of individual cells.

Relations Between Connectivity Styles and Active Information Storage

We focused in this study on the dynamics of links of information sharing. Information sharing can be seen as a generalized measure of cross-correlation between the firing activity of two different single units (see *Methods*). In Clawson et al. (2019), we analyzed as well *active information storage* (Lizier, Atay, & Jost, 2012), a complementary measure, which can be seen as a generalized autocorrelation of the firing activity of a single node (or, equivalently, to a self-loop of information sharing connectivity). While information sharing quantifies the amount of information in common between the present activity of a neuron and the past activity of another, information storage is meant to capture the amount of information in the present activity of a neuron that was already conveyed by its past activity (see *Methods*). In this sense, neurons with a large value of information storage would functionally act as "memory buffers" repeating in time the same information content (cf. *Discussion*). In Clawson et al. (2019) we found that information storage, as information sharing, is state-dependent and that some cells, which we called therein "storage hubs," display particularly large values of storage. We checked here whether high storage cells manifest some preferential connectivity style.

We show in Supporting Figure S9 distributions of information storage values, separated according to the connectivity style assumed by different neurons in each different network state. We found that high storage is not associated exclusively with specific styles of connectivity. On the contrary, cells with high storage could be found for any of the connectivity styles. The overall larger storage values were found for core streamers cells. However, we could find high storage cells even among the core-skin helpers and the periphery callers. Interestingly, distributions of storage for core-skin and periphery styles were bimodal, including a peak at high storage values (see *Discussion* for possible interpretations).

DISCUSSION

We have described here the internal organization of assemblies of neurons dynamically exchanging information through time, using a temporal network framework and developing adequate tools for their analysis. In line with our previous study (Clawson et al., 2019), we found a coexistence of organization, such as the existence of discrete network states, and freedom, such as the liquid continuous reorganization of network neighborhoods within each state. The rich information sharing dynamics we revealed in our anesthesia recordings in hippocampus and entorhinal cortex cannot be explained merely in terms of transitions between global brain states (here, alternations between "REM-sleep"-like THE epochs and SO epochs). On the contrary, we found that each of the global state gives access to wide repertoires of possible networks of information sharing between neurons. These network state repertoires are largely global state-specific and are robustly identified using both weighted and unweighted network characterizations.

We extracted here functional connectivity networks evaluating information sharing—that is, time-lagged mutual information—between the firing of pairs of single units. This choice was motivated by the fact that mutual information is relatively simpler to evaluate than other more sophisticated and explicitly directed measures of information transfer (Schreiber, 2000), which require larger amounts of data to be properly estimated. Using a simpler measure was thus better suited to our need to estimate connectivity within short windows, to give rise to a temporal network description. Although mutual information is a symmetric measure, the introduction of a time lag makes our metric "pseudodirected" because information cannot causally propagate from the future to the past. Therefore, sharing of information between the past activity of a node i and the present activity of another node j could be indicative of a flow of information

from i to j. When computing time-lagged mutual information between all directed pairs of single units in our recording, we found however only a very mild degree of asymmetry. As shown in Supporting Figure S8, most strong information sharing connections were very close to symmetric, indicative of time-lagged mutual information peaking near zero-lag for these connections. This finding corresponds to the early intuition that members of a cell assembly share information via their tightly synchronized firing (Abeles, 1982; Hebb, 1949). Supporting Figure S8 also shows that some of the more weakly connected pairs of neurons displayed a varying degree of directional asymmetry, with the strongest imbalance found for cells with a core connectivity style. However, the strengths of nodes with unbalanced pseudodirected sharing were orders of magnitude smaller than for balanced nodes. Our choice to ignore asymmetries thus appears well justified, as is the choice to use lagged mutual information rather than more complex directed metrics.

A striking architectural property of the measured information sharing networks was their core-periphery architecture. Such architecture was preserved at every time frame (as shown in Figure 3B), although the coreness of individual neurons changed smoothly through time even within states. This preservation of a global functional architecture despite the variation of the specific realizations and participant neurons is reminiscent of "functional homeostasis" observed in highly heterogeneous circuits that must nevertheless perform a crucial function in a stable and efficient manner (Kispersky, Gutierrez, & Marder, 2011; Marder & Goaillard, 2006). What is important is that, at any time, a functional separation between "streamers," "helpers," or "callers" exists, however which neurons specifically assume these roles and the exact location of these neurons within the anatomical circuit (cf. Figure 5D) appear to be less important.

Core-periphery organizations have been found in many social, infrastructure, communication, and information processing networks, with various types of coreness profiles, that is, strong or gradual separations between the innermost core and the most peripheral nodes (Della Rossa et al., 2013; Holme, 2005; Kojaku & Masuda, 2018; Puck Rombach, Porter, Fowler, & Mucha, 2014). The dynamics of this type of structure has however barely been tackled in temporal networks (Galimberti et al., 2018). In neuroscience, such architecture has been identified in larger-scale networks of interregional functional connectivity, during both task and rest (Avena-Koenigsberger, Misic, & Sporns, 2017; Bassett et al., 2013; Battiston, Guillon, Chavez, Latora, & Fallani, 2018; de Pasquale, Corbetta, Betti, & Penna, 2018), in line with the general idea that cognition requires the formation of integrated coalitions of regions, merging information streams first processed by segregated subsystems (Deco, Tononi, Boly, & Kringelbach, 2015; Tononi, Edelman, & Sporns, 1998). Here, we find that a similar architecture is prominent at the completely different scale of networks between single units within local microcircuits in the hippocampal formation. The core-periphery architecture of information sharing thus reflects dynamic information integration and segregation. Cells belonging to the core form an integrated ensemble, within which strong flows of information are continually streamed and echoed. At the opposite end of the hierarchy of connectivity styles, peripheral neurons are segregated and perform transient "calls" toward "streamer" neurons in the core to get updated and share their specific information contents.

Following Buzsáki (2010), a "syntax of information processing" would be enforced by the spatiotemporal organization of neuronal firing. Our dynamic core-periphery architecture is also ultimately determined by the coordinated firing patterns of many neurons. The fact that these coordinated firing patterns invariantly translate into networks with a core-periphery architecture can be seen as a proxy for the existence of a syntactic organization of information

flows. In this self-organized syntax, peripheral neurons are in the ideal functional position to act as "readers" of the contents streamed by the integrated cell assembly formed by core neurons. Transitions between network states may act as the equivalent of bar lines, parsing the flow of information into "words" or longer sentence blocks, spelled with an irregular tempo. In the vision of Buzsáki (2010), roles such as the one of reader or chunking into informational words would be a by-product of neuronal firing organization. We thus stress here once again that even in our case the real "stuff" out of which sharing functional networks are made are spiking patterns at the level of the assembly. The network representation provides however a natural and intuitive visualization of the dynamics of these patterns. Coordinated firing events—and not single neuron firing properties, cf. the poor correlations in Supporting Figure S5—are mapped into network structures and changes of firing pattern into changes of connectivity style within the network. The logical syntax of assembly firing is thus translated into a dynamic topological architecture of sharing networks, which is easier to study and characterize.

In order to interpret the functional role of this emergent core-periphery organization, one should elucidate the information processing roles played by individual neurons within this network organization. An entire spectrum of possible roles may exist, mirroring the smooth separation subsisting between core and periphery. Communication between core and periphery can be helped by core-skin neurons, which sporadically connect to the core, transiently expanding its size. Speculatively, such breathing of the integrated core may be linked to fluctuating needs in terms of information processing bandwidth, analogous to dynamic memory allocation in artificial computing systems. The possible algorithmic role of neurons with different connectivity styles could be investigated using metrics from the partial information decomposition framework (Wibral, Priesemann, Kay, Lizier, & Phillips, 2017). Beyond pseudodirected sharing, it may be possible to identify neurons acting as active memory buffers displaying large information storage (Lizier et al., 2012); neurons actively transfering information to others, associated with large transfer entropy (Schreiber, 2000); or, yet, neurons combining received inputs into new, original representations, associated with positive information modification values (Lizier, Flecker, & Williams, 2013). As previously said, we could at least quantify information storage. In particular, as shown in Supporting Figure S9, subgroups of core-skin helpers and periphery callers existed with high storage values, approaching the ones of storage hubs within the core. Therefore, at least some of the core-skin or periphery cells transiently connected to the core may play the role of ancillary memory units, "flash drives" sporadically plugged in when needed to write or read specific information snippets. Unfortunately, the number of coordinated firing events observed in our recordings was not sufficient for a reasonable estimation of transfer or modification, beyond storage. We can nevertheless hypothesize that core neurons are the workhorses of information modification, shaping novel informational constructs via their integrated firing.

Encoding and retrieval:
Two components of the memory functions exerted by the hippocampus (and possibly different parts of it), with encoding corresponding to the "writing" of an internal memory and retrieval to the "reading" of existing memories.

We found that the bursty core-skin style—the "freelancer helper" role—was over-represented in SR of CA1 and Layer 2 of EC. SR receives inputs from hippocampus CA3 that are believed to be linked to retrieval of previously encoded associations (Hasselmo & Stern, 2013; Schomburg et al., 2014). CA3, an associative memory module crucial for retrieval, receives inputs on its turn from layer 2 of EC. The overrepresentation of the bursty core-skin style in SR and Layer 3 of EC may thus be compliant with our intuition of "helpers" as additional on-demand storage resources, plugged to the core when needed to read the specific contents buffered by their spiking. On the contrary, Layer 3 of EC, which sends inputs to stratum lacunosum-moleculare of CA1, would rather mediate encoding than retrieval (Douchamps, Jeewajee, Blundell, Burgess, & Lever, 2013; Schomburg et al., 2014). Correspondingly, in Layer 3 of EC the overrepresentation of freelancer helpers observed in Layer 2 is replaced by an underrepresentation,

consistently with the complementary functions that inputs from these EC layers are postulated to play.

We also found an excess of inhibitory interneurons among core style cells (Figure 5D). Inteneurons tended to exhibit larger firing rates than excitatory cells, but we showed that coreness is not significantly affected by firing rate (Supporting Figure S5C). Therefore, this excess is rather to be linked to a key functional role of interneurons in mediating cell assembly formation. Their central position within the core of the information sharing network may allow them to efficiently control the recruitment of new neurons into the integrated core and orchestrate their coordinated firing, as already discussed in the literature (Bonifazi et al., 2009; Quilichini et al., 2012).

Remarkably, however, in a majority of cases, the connectivity style adopted by a neuron was only poorly affected by its anatomical localization or by its cell type. Apart from the few exceptions just discussed above, the distribution of the different styles through the different anatomical regions and layers was indeed close to chance levels. In particular, the fact of being localized within a specific layer of CA1 or EC did not affect in a significant way the probability of belonging to the core or to the periphery. Furthermore, a majority of neurons switched between different styles when network state changed (Figure 6), indicating that connectivity styles and, in particular, core membership are not hardwired. In contrast, it is often thought that the function that a neuron plays is affected by its individual firing and morphology properties, as well as by details of its synaptic connections within the circuit (Booker & Vida, 2018). In this dominating view, functional hubness would thus be the garland reserved for a few elite cells, selected because of their extreme technical specialization, largely determined by their developmental lineage (Cossart, 2014). Here—further elaborating on Clawson et al. (2019)—we propose a more "democratic" view in which core membership and, more in general, connectivity style would be dynamically appointed, such that the total number of neurons that are elected into the core at least once is much larger than the currently active core members at specific times. The core composition can indeed be radically reorganized when the network states switch and can fluctuate between alternative majorities of hippocampal or entorhinal cortex neurons (Figure 3D).

Such a democratic system implies a primacy of collective dynamics at the neuronal population level, flexibly shaping coordinated firing ensembles, on technical specialization and "blood" origins at the single neuron level. Switching network states may reflect transitions between alternative attractors of firing dynamics (Amit, 1989) implementing alternative firing correlations. Discrete state switching coexists however with more liquid fluctations of core attachment, which would rather suggest a complex but not random dynamics at the edge of instability (Maass, Natschlager, & Markram, 2002; Marre, Yger, Davison, & Fregnac, 2009). State transitions and flexible core-periphery reorganization are also poorly determined by global oscillations, despite the important role played by oscillations in information routing (Buzsáki, 2006; Womelsdorf et al., 2007). Even if global oscillatory modes do not "freeze" information sharing patterns they nevertheless affect them, with different oscillatory states giving rise to alternative repertoires of possible information sharing networks (Figure 4D). Computational modeling of spiking neural circuits may help in the future to reach a mechanistic understanding of how ongoing collective oscillations interact with discrete attractor switching, metastable transients, and plasticity to give rise to liquid core-periphery architectures of information sharing.

We have started here applying a temporal network language to describe the internal life of cell assemblies along their emergence, expansion and contraction, and sudden transformations. We chose here to focus on an anesthesia condition in which intrinsic information

processing is not suppressed but considerably "slowed down" with respect to behavior, for methodological convenience (possibility to use long time windows for network estimation). In Clawson et al. (2019), we performed related analyses of information dynamics in natural sleep as well, again finding discrete state switching not only in the hippocampal formation but also in the prefrontal cortex. It will be interesting to consider in the future comparisons with additional conditions, as well as more detailed investigations of relations between network state dynamics and oscillatory dynamics or, even, actual behavior. In perspective, for instance, our method could be extended to recordings in pathological conditions—such as epilepsy, in which intrinsic assembly dynamics is altered (Muldoon, Soltesz, & Cossart, 2013)—relating temporal network properties' alterations to the degree of cognitive deficits. Furthermore, it may be possible to relate network state transitions within consistent oscillatory epochs (e.g., THE) to changes of the cross-frequency coupling between theta and gamma oscillations, since multiple gamma oscillations types are known to exist and be linked to alternative cognitive processes (Schomburg et al., 2014). To cope, however, with the much faster timescales relevant for behavioral tasks, we should modify our network estimation approach to avoid the use of too-short windows. Nevertheless, information sharing networks could be estimated first in a state-resolved manner, by pooling together firing events based on the similarity of the conditions in which they occur—for example, transient phase relations and synchrony levels (Palmigiano, Geisel, Wolf, & Battaglia, 2017) or coactivation patterns (Malvache et al., 2016; Miller et al., 2014)—rather than strict temporal contiguity. State-specific network frames could then be reallocated to specific times, depending on which "state" the system is visiting at different times, thus reconstructing an effective temporal network with the same time resolution as the original recordings (see, e.g., Thompson et al., 2017, for an analogous approach used at the macroscale of fMRI signals). In this way it would become possible to link temporal network reconfiguration events to actual behavior, hence probing their direct functional relevance.

METHODS

Animal Surgery

In this work we used a portion of the data (12 of 18 experiments) initially published by Quilichini et al. (2010), which includes local field potentials (LFPs) and single-unit recordings obtained from the dorsomedial entorhinal cortex of anesthetized rats. Seven additional simultaneous recordings in both mEC and dorsal HPC under anesthesia were included in this study, previously analyzed by Clawson et al. (2019). Details of anatomical locations and numbers of cells included can be found in Supporting Figure S1 and Supporting Table S1.

All experiments were in accordance with experimental guidelines approved by the Rutgers University (Institutional Animal Care and Use Committee) and Aix-Marseille University Animal Care and Use Committee. We performed experiments on 12 male Sprague Dawley rats (250 to 400 g; Hilltop Laboratory Animals) and 7 male Wistar Han IGS rats (250 to 400 g; Charles Rivers Laboratories). We performed acute experiments anesthetizing these rats with urethane (1.5 g/kg, intraperitoneally) and ketamine/xylazine (20 and 2 mg/kg, intramuscularly), with additional doses of ketamine/xylazine (2 and 0.2 mg/kg) being supplemented during the electrophysiological recordings to avoid recovery from anesthesia. The body temperature was monitored and kept constant with a heating pad. The head was secured in a stereotaxic frame (Kopf) and the skull was exposed and cleaned. Two miniature stainless steel screws, driven into the skull, served as ground and reference electrodes. To reach the mEC, we performed one craniotomy from bregma: −7.0 mm anteroposterior (AP) and +4.0 mm mediolateral (ML); to reach the CA1 area of HPC, we performed one craniotomy from bregma: 3.0 mm AP and +2.5 mm ML. The probes were mounted on a stereotaxic arm. We recorded the dorsomedial

portion of the mEC activity using a NeuroNexus CM32-4×8-5 mm-Buzsaki32-200-177 probe (in eight experiments), a 10-mm-long Acreo single-shank silicon probe with 32 sites (50-mm spacing) arranged linearly (in five experiments), or a NeuroNexus H32-10mm-50-177 probe (in five experiments), which was lowered in the EC at 5.0 to 5.2 mm from the brain surface with a 20° angle. We recorded HPC CA1 activity using a H32-4×8-5mm-50-200-177 probe (NeuroNexus Technologies) lowered at 2.5 mm from the brain surface with a 20° angle (in four experiments), a NeuroNexus H16-6mm-50-177 probe lowered at 2.5 mm from the brain surface with a 20° angle (in two experiments). The online positioning of the probes was assisted by the presence of unit activity in cell body layers and the reversal of theta oscillations when passing from L2 to L1 for the mEC probe and the presence in SP of either unit activity or ripples (80 to 150 Hz) for the HPC probe.

At the end of the recording, the animals were injected with a lethal dose of pentobarbital Na (150 mg/kg, intraperitoneally) and perfused intracardially with 4% paraformaldehyde solution. We confirmed the position of the electrodes (DiI was applied on the back of the probe before insertion) histologically on Nissl-stained 40-mm section.

Data Collection and Spike Sorting

Extracellular signal recorded from the silicon probes was amplified (1,000), bandpass-filtered (1 Hz to 5 kHz), and acquired continuously at 20 kHz with a 64-channel DataMax System (RC Electronics ora 258-channel Amplipex) or at 32 kHz with a 64-channel DigitalLynx (NeuraLynx at 16-bit resolution). We preprocessed raw data using a custom-developed suite of programs (Csicsvari, Hirase, Czurka, Mamiya, & Buzsaki, 1999). After recording, the signals were downsampled to 1250 Hz for the LFP analysis. Spike sorting was performed automatically using KLUSTAKWIK (`http://klustakwik.sourceforge.net`, Harris, Henze, Csicsvari, Hirase, & Buzsáki, 2000), followed by manual adjustment of the clusters, with the help of autocorrelogram, cross-correlogram (CCG), and spike waveform similarity matrix (KLUSTERS software package; `https://klusta.readthedocs.io/en/latest/`, Hazan, Zugaro, & Buzsáki, 2006). After spike sorting, we plotted the spike features of units as a function of time and discarded the units with signs of significant drift over the period of recording. Moreover, we included in the analyses only units with clear refractory periods and well-defined clusters.

Recording sessions were divided into brain states of THE and SO periods. The epochs of stable theta (THE) or slow oscillations (SO) were visually selected from the ratios of the whitened power in the THE band ([3 6] Hz in anesthesia) and the power of the neighboring bands of EC Layer 3 LFP, which was a layer present in all of the 18 anesthesia recordings.

We determined the layer assignment of the neurons from the approximate location of their somata relative to the recording sites (with the largest amplitude unit corresponding to the putative location of the soma), the known distances between the recording sites, and the histological reconstruction of the recording electrode tracks. To assess the excitatory or inhibitory nature of each of the units, we calculated pairwise cross-correlograms between spike trains of these cells. We determined the statistical significance of putative inhibition or excitation (trough or peak in the [+2:5] ms interval, respectively) using well-established nonparametric tests and criteria used for identifying monosynaptic excitations or inhibitions (Quilichini et al., 2010), in which each spike of each neuron was jittered randomly and independently on a uniform interval of [5:5] ms a thousand times to form 1,000 surrogate datasets and from which the global maximum and minimum bands at 99% acceptance levels were constructed.

Information Sharing Networks

We estimated time-resolved information sharing networks following the same procedures as Clawson et al. (2019). In particular, we used *time-lagged mutual information* between binarized spike trains as a measure of the amount of *shared information*. Information sharing between each pair of neurons $(i, j)_{i,j=1,\ldots,N}$ is defined as the time-lagged mutual information $MI[i(t), j(t-\lambda)]$ between the firing patterns extracted for the relative neurons in a 10-s-long time window:

$$I_{shared}(j \to i) = \sum_{\lambda} MI[i(t), j(t-\lambda)] \ , \tag{1}$$

$$I_{shared}(i \to j) = \sum_{\lambda} MI[j(t), i(t-\lambda)] \ , \tag{2}$$

where the time lag λ varies in the range $0 \leq \lambda \leq 0.5T^{\theta}$, T^{θ} being the phase of the THE cycle (THE oscillations have higher frequency than slow oscillations). We subtract a significance threshold, that is, the 95th percentile of MI computed on reshuffled binarized spike trains (400 iterations), setting to zero non-significant terms. The information sharing network is defined by an adjacency matrix $A(i, j)_{i,j=1,\ldots,N}$, whose element $A(i, j)$ corresponds to $I_{shared}(i \to j)$. It is therefore a weighted, directed network. The time window is then shifted by 1 s to extract the information sharing network at the next time-step, assuring a 90% overlap with the previous time window for the computation of the information theoretic measures.

In order to study the effect of asymmetries in the adjacency matrices of our information sharing networks, we compute the *asymmetry coefficient* $\Delta S\%$ for each neuron in each state h, defined as follows:

$$\Delta S\%_h^i = \frac{s_{out}^{i,h} - s_{in}^{i,h}}{s_{out}^{i,h} + s_{in}^{i,h}}, \quad \forall i = 1, \ldots, N \ . \tag{3}$$

$\Delta S\%_h^i$ thus represents the ratio between the amount of information that neuron i outputs to other neurons during state h ($s_{out}^{i,h} = \sum_{t=1,\ldots,T^h} \sum_j w_{ij}$) and the amount of information that is conveyed to neuron i by its neighbors during state h ($s_{in}^{i,h} = \sum_{t=1,\ldots,T^h} \sum_j w_{ji}$). $\Delta S\%_h^i = 1$ means that for neuron i in state h, $s_{in}^{i,h} = 0$, therefore it is a perfect *sender* of information, whereas if $\Delta S\%_h^i = -1$, $s_{out}^{i,h} = 0$ and the neuron is therefore a perfect *receiver*. If $\Delta S\%_h^i = 0$, then $s_{out}^{i,h} = s_{in}^{i,h}$ and therefore the amount of information that neuron i conveys to its neighbors during the state h is equal to the amount of information that it receives. As shown in Supporting Figure S10, the asymmetries in the adjacency matrices of the information sharing networks have a negligible effect. We thus neglect the aforementioned asymmetries and consider the networks to be undirected.

Active Information Storage

Information sharing can be seen as a generalized form of cross-correlation where the time-lagged mutual information captures all types of linear and nonlinear correlations. Analogously, one can evaluate a generalized autocorrelation functional, known under the name of active information storage (Lizier et al., 2012). Following Clawson et al. (2019), we evaluated active information storage of a given neuron, within a given time window as

$$I_{storage}(i) = \sum_{\lambda} MI[i(t), i(t-\lambda)] \ , \tag{4}$$

where the time lag λ varies once again in the range $0 \leq \lambda \leq 0.5T^{\theta}$. The values of storage whose distributions are shown in Supporting Figure S9 are averages for each neuron over all the time windows whose associated connectivity profile match a specific connectivity style (see below for definitions of connectivity profiles and styles).

Network Features

As described in the main text, we consider the cosine similarity and Jaccard coefficient between the neighborhoods of each node in successive times. See the jargon boxes for the precise definitions.

We also consider the definition of *coreness* C^i of node i in a network introduced by Della Rossa et al. (2013), see the jargon box in the main text. To compute the coreness of neurons at each time frame we used the implementation of the method available at `https://core-periphery-detection-in-networks.readthedocs.io/en/latest/index.html`.

Null Models

We compare the results obtained in the empirical data to those achieved by repeating the presented analysis on three different null models obtained by different randomization procedures of the original networks:

- Random null model: Temporal network obtained by generating at each time step t an Erdös-Rényi random graph with the same number of nodes and edges as the original data.
- Degree-preserving null model: Temporal network generated by randomizing at each time t the edges of the original network at the corresponding time, preserving the degree (number of connections) of each node. To this aim we use the method of Maslov and Sneppen (2002).
- Neighborhood-preserving null model: A temporal network whose adjacency matrix at time t is obtained by a systematic reshuffling of the weights of the experimental data temporal network; this preserves the neighborhood (set of neighbors) of each node at each time. This randomization procedure therefore leaves the unweighted structure unchanged.

Network States

The two pairs of feature vectors computed at each time t, two vectors for the unweighted case and two for the weighted one, are merged into two $2 \times N$-dimensional vectors, one containing the unweighted features (Jaccard and unweighted coreness) and the other formed by the weighted ones (cosine similarity and weighted coreness). For each recording we therefore have two series of length T (T varies for different recordings), of weighted and unweighted feature vectors. In order to investigate the existence of recurring epochs of stable (correlated) liquidity and topology configuration of the network (the *network states*), we perform a K-means clustering on the feature vector time series. As a result of the clustering we obtain for each recording two sets (one for the weighted analysis, one for the unweighted one) of network states of specific liquidity (Jaccard index, for unweighted networks, or cosine similarity, for weighted networks) and core-periphery organization (unweighted or unweighted coreness) of the system (Figure 4A).

Network States Obtained From Global Network Features

We consider six *global* network features, three for the unweighted case and three for the weighted case: the node-averaged cosine similarity (Jaccard index in the unweighted case); the node averaged coreness (weighted and unweighted); and the sum over all weights of all edges (number of edges in the unweighted case). These features are computed at each time t and merged in two 3-dimensional vectors, yielding two time series of length T for each recording (where T varies for each recording). As for the local network feature vectors, we perform a K-means clustering on each (unweighted and weighted) feature vector time series: As a result, we obtain for each recording the two sets of global unweighted and weighted network states, corresponding to the epochs of similar organization of the network in terms of node-averaged liquidity, core-periphery structure, and connectivity.

Clustering Connectivity Profiles: Connectivity Styles

As shown in Figure 5B, we represent the connectivity behavior of a neuron in a network state with a radar plot whose radial axes correspond to the six features defined in the *Results* section, which are averages of temporal properties over the network state. We therefore compute one 6-dimensional *connectivity profile* for each neuron, in each network state, for each recording. We investigate the existence of typical connectivity profiles across different recordings: this corresponds to searching for common radar plot shapes for neurons of different network states of different recordings. We therefore perform a K-means clustering on all the connectivity profiles computed for each neuron, in each network state, in each recording: We obtain four cluster of connectivity profiles, which name *connectivity styles*. These connectivity styles are shown in Figure 5B and interpreted in the *Results* and *Discussion* sections.

Unsupervised Classification for Soft Labeling of Connectivity Profile

We use the K-nearest-neighbor unsupervised classification method, trained on the connectivity style labels of all the connectivity profiles, to obtain a soft classification of each neuron's connectivity profile. Each neuron's state-averaged connectivity profile's soft label is represented by a 4-dimensional normalized vector: Each component of this vector represents the probability of the connectivity profile to belong to the corresponding connectivity style (core, periphery, bursty core-skin, regular core-skin). The connectivity styles shown in Figure 5B correspond to the connectivity profiles of maximum probability to belong to the connectivity style of the corresponding color, that is, of maximum soft label component of the corresponding connectivity style. The soft classification of connectivity profiles is graphically represented in Figure 5C by plotting the connectivity profiles' vectors of connectivity style soft labels in a 3-dimensional space. In order to achieve a clearer visual representation, the probabilities of belonging to the regular core-skin or the bursty core-skin connectivity styles have been summed into a single component of the soft label vector.

Cross–Network State Connectivity Profile Transition Rate

The cross–network state connectivity profile transition rate η^i of neuron i is defined as

$$\eta^i \equiv \frac{\#\ profile\ transitions\ of\ node\ i}{max(\#\ global\ classes,\ \#\ network-states)}. \tag{5}$$

It quantifies the tendency of neuron i to switch, often or rarely, between connectivity profiles belonging to different connectivity styles in different states: When $\eta^i = 1$, neuron i switches connectivity style at every change of network state; when $\eta^i = 0$, neuron i is always in the same connectivity style.

SUPPORTING INFORMATION

Supporting information for this article is available at https://doi.org/10.1162/netn_a_00142.

AUTHOR CONTRIBUTIONS

Nicola Pedreschi: Conceptualization; Investigation; Methodology; Software; Visualization; Writing - Original Draft; Writing - Review & Editing. Christophe Bernard: Data curation; Resources; Writing - Review & Editing. Wesley Clawson: Data curation; Formal analysis; Resources; Writing - Review & Editing. Pascale Quilichini: Data curation; Resources; Writing - Review & Editing. Alain Barrat: Conceptualization; Methodology; Supervision; Writing - Original Draft; Writing - Review & Editing. Demian Battaglia: Conceptualization; Methodology; Supervision; Writing - Original Draft; Writing - Review & Editing.

FUNDING INFORMATION

Nicola Pedreschi, H2020 Marie Skłodowska-Curie Actions (http://dx.doi.org/10.13039/100010665), Award ID: 713750. Nicola Pedreschi, Regional Council of Provence-Alpes-Côte d'Azur and A*MIDEX, Award ID: ANR-11-IDEX-0001-02. Alain Barrat, Agence Nationale de la Recherche (http://dx.doi.org/10.13039/501100001665), Award ID: ANR-19-CE46-0008. Christophe Bernard, H2020 Marie Skłodowska-Curie Actions (http://dx.doi.org/10.13039/100010665), Award ID: 765549. Wesley Clawson, H2020 Marie Skłodowska-Curie Actions (http://dx.doi.org/10.13039/100010665), Award ID: 765549. Demian Battaglia, Centre National de la Recherche Scientifique (http://dx.doi.org/10.13039/501100004794), Award ID: INFINITI (Braintime Project). Alain Barrat, Centre National de la Recherche Scientifique (http://dx.doi.org/10.13039/501100004794), Award ID: INFINITI (Braintime project). Pascale Quilichini, CURE, Award ID: Epilepsy Taking Flight Award.

REFERENCES

Abeles, M. (1982). *Local cortical circuits, an electrophysiological study*. Berlin, Germany: Springer.

Aertsen, A. M., Gerstein, G. L., Habib, M. K., & Palm, G. (1989). Dynamics of neuronal firing correlation: modulation of "effective connectivity." *Journal of Neurophysiology*, *61*(5), 900–917.

Amit, D. J. (1989). *Modeling brain function: The world of attractor neural networks*. New York, NY: Cambridge University Press.

Avena-Koenigsberger, A., Misic, B., & Sporns, O. (2017). Communication dynamics in complex brain networks. *Nature Reviews Neuroscience*, *19*(1), 17–33. https://doi.org/10.1038/nrn.2017.149

Barabási, A. L. (2005). The origin of bursts and heavy tails in human dynamics. *Nature*, *435*, 207–211.

Bassett, D. S., Wymbs, N. F., Rombach, M. P., Porter, M. A., Mucha, P. J., & Grafton, S. T. (2013). Task-based core-periphery organization of human brain dynamics. *PLoS Computational Biology*, *9*(9), e1003171.

Battaglia, D., Karagiannis, A., Gallopin, T., Gutch, H. W., & Cauli, B. (2013). Beyond the frontiers of neuronal types. *Frontiers in Neural Circuits*, *7*, 13. https://doi.org/10.3389/fncir.2013.00013

Battiston, F., Guillon, J., Chavez, M., Latora, V., & Fallani, F. D. V. (2018). Multiplex core-periphery organization of the human connectome. *Journal of the Royal Society Interface*, *15*(146), 20180514. https://doi.org/10.1098/rsif.2018.0514

Bonifazi, P., Goldin, M., Picardo, M. A., Jorquera, I., Cattani, A., Bianconi, G., . . . Cossart, R. (2009). GABAergic hub neurons orchestrate synchrony in developing hippocampal networks. *Science*, *326*(5958), 1419–1424. https://doi.org/10.1126/science.1175509

Booker, S. A., & Vida, I. (2018). Morphological diversity and connectivity of hippocampal interneurons. *Cell and Tissue Research*, *373*(3), 619–641. https://doi.org/10.1007/s00441-018-2882-2

Buzsáki, G. (2006). *Rhythms of the brain*. New York, NY: Oxford University Press.

Buzsáki, G. (2010). Neural syntax: Cell assemblies, synapsembles, and readers. *Neuron*, *68*(3), 362–385. https://doi.org/10.1016/j.neuron.2010.09.023

Buzsáki, G., & Moser, E. I. (2013). Memory, navigation and theta rhythm in the hippocampal-entorhinal system. *Nature Neuroscience*, *16*(2), 130–138. https://doi.org/10.1038/nn.3304

Calhoun, V. D., Miller, R., Pearlson, G., & Adalı, T. (2014). The chronnectome: Time-varying connectivity networks as the next frontier in fMRI data discovery. *Neuron*, *84*(2), 262–274.

Cattuto, C., Van den Broeck, W., Barrat, A., Colizza, V., Pinton, J.-F., & Vespignani, A. (2010). Dynamics of person-to-person interactions from distributed RFID sensor networks. *PLoS ONE*, *5*(7), 1–9. https://doi.org/10.1371/journal.pone.0011596

Clawson, W., Vicente, A. F., Ferraris, M., Bernard, C., Battaglia, D., & Quilichini, P. P. (2019). Computing hubs in the hippocampus and cortex. *Science Advances*, *5*(6).

Cossart, R. (2014). Operational hub cells: A morpho-physiologically diverse class of GABAergic neurons united by a common function. *Current Opinion in Neurobiology*, *26*, 51–56. https://doi.org/10.1016/j.conb.2013.12.002

Csicsvari, J., Hirase, H., Czurka, A., Mamiya, A., & Buzsaki, G. (1999). Oscillatory coupling of hippocampal pyramidal cells and interneurons in the behaving rat. *Journal of Neuroscience*, *19*(1), 274–287. https://doi.org/10.1523/jneurosci.19-01-00274.1999

Darst, R. K., Granell, C., Arenas, A., Gómez, S., Saramäki, J., & Fortunato, S. (2016). Detection of timescales in evolving complex systems. *Scientific Reports*, *6*, 39713. https://doi.org/10.1038/srep39713

Deco, G., Tononi, G., Boly, M., & Kringelbach, M. L. (2015). Rethinking segregation and integration: Contributions of whole-brain modelling. *Nature Reviews Neuroscience*, *16*(7), 430–439. https://doi.org/10.1038/nrn3963

Della Rossa, F., Dercole, F., & Piccardi, C. (2013). Profiling core-periphery network structure by random walkers. *Scientific Reports*, *3*, 1467.

de Pasquale, F., Corbetta, M., Betti, V., & Penna, S. D. (2018). Cortical cores in network dynamics. *NeuroImage*, *180*, 370–382. https://doi.org/10.1016/j.neuroimage.2017.09.063

Douchamps, V., Jeewajee, A., Blundell, P., Burgess, N., & Lever, C. (2013). Evidence for encoding versus retrieval scheduling in the hippocampus by theta phase and acetylcholine. *Journal of Neuroscience*, *33*(20), 8689–8704. https://doi.org/10.1523/jneurosci.4483-12.2013

Forsyth, D. (2018). *Probability and statistics for computer science*. Berlin, Gemany: Springer.

Galimberti, E., Barrat, A., Bonchi, F., Cattuto, C., & Gullo, F. (2018). Mining (maximal) span-cores from temporal networks. In *Proceedings of the 27th ACM international Conference on Information and Knowledge Management* (pp. 107–116).

Gauvin, L., Panisson, A., & Cattuto, C. (2014). Detecting the community structure and activity patterns of temporal networks: A non-negative tensor factorization approach. *PLoS ONE*, *9*(1), e86028.

Gelardi, V., Fagot, J., Barrat, A., & Claidière, N. (2019). Detecting social (in)stability in primates from their temporal co-presence network. *Animal Behaviour*, *139*, 239.

Gilbert, C. D., & Sigman, M. (2007). Brain states: Top-down influences in sensory processing. *Neuron*, *54*(5), 677–696. https://doi.org/10.1016/j.neuron.2007.05.019

Harris, K. D., Henze, D. A., Csicsvari, J., Hirase, H., & Buzsáki, G. (2000). Accuracy of tetrode spike separation as determined by simultaneous intracellular and extracellular measurements. *Journal of Neurophysiology*, *84*(1), 401–414. https://doi.org/10.1152/jn.2000.84.1.401

Hasselmo, M. E., & Stern, C. E. (2013). Theta rhythm and the encoding and retrieval of space and time. *NeuroImage*, *85*(Pt. 2), 656–666. https://doi.org/10.1016/j.neuroimage.2013.06.022

Hazan, L., Zugaro, M., & Buzsáki, G. (2006). Klusters, NeuroScope, NDManager: A free software suite for neurophysiological data processing and visualization. *Journal of Neuroscience Methods*, *155*(2), 207–216. https://doi.org/10.1016/j.jneumeth.2006.01.017

Hebb, D. (1949). *The organization of behavior: A neuropsychological theory*. New York, NY: Wiley.

Holme, P. (2005). Core-periphery organization of complex networks. *Physical Review E*, *72*, 046111. https://doi.org/10.1103/PhysRevE.72.046111

Holme, P. (2015). Modern temporal network theory: A colloquium. *European Physical Journal B*, *88*(9), 234.

Holme, P., & Saramäki, J. (2012). Temporal networks. *Physics Reports*, *519*(3), 97–125. https://doi.org/10.1016/j.physrep.2012.03.001

Hutchison, R. M., Womelsdorf, T., Allen, E. A., Bandettini, P. A., Calhoun, V. D., Corbetta, M., . . . Chang, C. (2013). Dynamic functional connectivity: Promise, issues, and interpretations. *Neuroimage*, *80*, 360–378.

Ikegaya, Y., Aaron, G., Cossart, R., Aronov, D., Lampl, I., Ferster, D., & Yuste, R. (2004). Synfire chains and cortical songs: Temporal modules of cortical activity. *Science*, *304*(5670), 559–564. https://doi.org/10.1126/science.1093173

Kirst, C., Timme, M., & Battaglia, D. (2016). Dynamic information routing in complex networks. *Nature Communications*, *7*(1), 11061. https://doi.org/10.1038/ncomms11061

Kispersky, T., Gutierrez, G. J., & Marder, E. (2011). Functional connectivity in a rhythmic inhibitory circuit using Granger causality. *Neural Systems and Circuits*, *1*(1), 9. https://doi.org/10.1186/2042-1001-1-9

Klausberger, T., Magill, P. J., Márton, L. F., Roberts, J. D. B., Cobden, P. M., Buzsáki, G., & Somogyi, P. (2003). Brain-state- and cell-type-specific firing of hippocampal interneurons in vivo. *Nature*, *421*(6925), 844–848. https://doi.org/10.1038/nature01374

Kobayashi, T., Takaguchi, T., & Barrat, A. (2019). The structured backbone of temporal social ties. *Nature Communications*, *10*(1), 220.

Kojaku, S., & Masuda, N. (2018). Core-periphery structure requires something else in the network. *New Journal of Physics*, *20*(4), 043012. https://doi.org/10.1088/1367-2630/aab547

Kovanen, L., Karsai, M., Kaski, K., Kertész, J., & Saramäki, J. (2011). Temporal motifs in time-dependent networks. *Journal of Statistical Mechanics*, P11005.

Laurent, G., Saramäki, J., & Karsai, M. (2015). From calls to communities: A model for time-varying social networks. *European Physial Journal B*, *88*, 301.

Lizier, J. T., Atay, F. M., & Jost, J. (2012). Information storage, loop motifs, and clustered structure in complex networks. *Physical Review E*, *86*(2), 026110. https://doi.org/10.1103/physreve.86.026110

Lizier, J. T., Flecker, B., & Williams, P. L. (2013). Towards a synergy-based approach to measuring information modification. *2013 IEEE Symposium on Artificial Life*, 43–51. https://doi.org/10.1109/alife.2013.6602430

Maass, W., Natschlager, T., & Markram, H. (2002). Real-time computing without stable states: A new framework for neural computation based on perturbations. *Neural Computation*, *14*(11), 2531–2560. https://doi.org/10.1162/089976602760407955

Malvache, A., Reichinnek, S., Villette, V., Haimerl, C., & Cossart, R. (2016). Awake hippocampal reactivations project

onto orthogonal neuronal assemblies. *Science*, *353*(6305), 1280–1283. https://doi.org/10.1126/science.aaf3319

Mao, B.-Q., Hamzei-Sichani, F., Aronov, D., Froemke, R. C., & Yuste, R. (2001). Dynamics of spontaneous activity in neocortical slices. *Neuron*, *32*(5), 883–898. https://doi.org/10.1016/s0896-6273(01)00518-9

Marder, E., & Goaillard, J.-M. (2006). Variability, compensation and homeostasis in neuron and network function. *Nature Reviews Neuroscience*, *7*(7), 563–574. https://doi.org/10.1038/nrn1949

Marre, O., Yger, P., Davison, A. P., & Fregnac, Y. (2009). Reliable recall of spontaneous activity patterns in cortical networks. *Journal of Neuroscience*, *29*(46), 14596–14606. https://doi.org/10.1523/jneurosci.0753-09.2009

Maslov, S., & Sneppen, K. (2002). Specificity and stability in topology of protein networks. *Science*, *296*(5569), 910–913. https://doi.org/10.1126/science.1065103

Masuda, N., & Holme, P. (Eds.). (2017). *Temporal network epidemiology*. Singapore: Springer.

Miller, J.-e. K., Ayzenshtat, I., Carrillo-Reid, L., & Yuste, R. (2014). Visual stimuli recruit intrinsically generated cortical ensembles. *Proceedings of the National Academy of Sciences*, *111*(38), E4053–E4061. https://doi.org/10.1073/pnas.1406077111

Miritello, G., Lara, R., Cebrian, M., & Moro, E. (2013). Limited communication capacity unveils strategies for human interaction. *Scientific Reports*, *3*(1), 1950. https://doi.org/10.1038/srep01950

Muldoon, S. F., Soltesz, I., & Cossart, R. (2013). Spatially clustered neuronal assemblies comprise the microstructure of synchrony in chronically epileptic networks. *Proceedings of the National Academy of Sciences*, *110*(9), 3567–3572. https://doi.org/10.1073/pnas.1216958110

Orlandi, J. G., Soriano, J., Alvarez-Lacalle, E., & Teller, S. (2013). Noise focusing and the emergence of coherent activity in neuronal cultures. *Nature Physics*, *9*(9). https://doi.org/10.1038/nphys2686

Palmigiano, A., Geisel, T., Wolf, F., & Battaglia, D. (2017). Flexible information routing by transient synchrony. *Nature Neuroscience*, *20*(7), 1014–1022. https://doi.org/10.1038/nn.4569

Poli, D., Pastore, V. P., & Massobrio, P. (2015). Functional connectivity in in vitro neuronal assemblies. *Frontiers in Neural Circuits*, *9*, 57. https://doi.org/10.3389/fncir.2015.00057

Puck Rombach, M., Porter, M., Fowler, J., & Mucha, P. J. (2014). Core-periphery structure in networks. *SIAM Journal on Applied Mathematics*, *74*, 167.

Quilichini, P., LeVanQuyen, M., Ivanov, A., Turner, D., Carabalona, A., Gozlan, H., . . . Bernard, C. (2012). Hub GABA neurons mediate gamma-frequency oscillations at ictal-like event onset in the immature hippocampus. *Neuron*, *74*(1), 57–64. https://doi.org/10.1016/j.neuron.2012.01.026

Quilichini, P., Sirota, A., & Buzsáki, G. (2010). Intrinsic circuit organization and theta-gamma oscillation dynamics in the entorhinal cortex of the rat. *Journal of Neuroscience*, *30*(33), 11128–11142. https://doi.org/10.1523/jneurosci.1327-10.2010

Saramäki, J., & Moro, E. (2015). From seconds to months: An overview of multi-scale dynamics of mobile telephone calls. *European Physical Journal B*, *88*, 164.

Schomburg, E. W., Fernandez-Ruiz, A., Mizuseki, K., Berenyi, A., Anastassiou, C. A., Koch, C. & Buzsáki, G. (2014). Theta phase segregation of input-specific gamma patterns in entorhinal-hippocampal networks. *Neuron*, *84*(2), 470–485. https://doi.org/10.1016/j.neuron.2014.08.051

Schreiber, T. (2000). Measuring Information Transfer. *Physical Review Letters*, *85*(2), 461–464. https://doi.org/10.1103/physrevlett.85.461

Stehlé, J., Charbonnier, F., Picard, T., Cattuto, C., & Barrat, A. (2013). Gender homophily from spatial behavior in a primary school: A sociometric study. *Social Networks*, *35*(4), 604–613. https://doi.org/10.1016/j.socnet.2013.08.003

Stetter, O., Battaglia, D., Soriano, J., & Geisel, T. (2012). Model-free reconstruction of excitatory neuronal connectivity from calcium imaging signals. *PLoS Computational Biology*, *8*(8), e1002653. https://doi.org/10.1371/journal.pcbi.1002653

Thompson, W. H., Brantefors, P., & Fransson, P. (2017). From static to temporal network theory: Applications to functional brain connectivity. *Network Neuroscience*, *1*, 69.

Tononi, G., Edelman, G. M., & Sporns, O. (1998). Complexity and coherency: Integrating information in the brain. *Trends in Cognitive Sciences*, *2*(12), 474–484. https://doi.org/10.1016/s1364-6613(98)01259-5

Valdano, E., Poletto, C., Giovannini, A., Palma, D., Savini, L., & Colizza, V. (2015). Predicting epidemic risk from past temporal contact data. *PLoS Computational Biology*, *11*(3), 1–19. https://doi.org/10.1371/journal.pcbi.1004152

Varela, F., Lachaux, J.-P., Rodriguez, E., & Martinerie, J. (2001). The brainweb: Phase synchronization and large-scale integration. *Nature Reviews Neuroscience*, *2*(4), 229–239. https://doi.org/10.1038/35067550

Wibral, M., Priesemann, V., Kay, J. W., Lizier, J. T., & Phillips, W. A. (2017). Partial information decomposition as a unified approach to the specification of neural goal functions. *Brain and Cognition*, *112*, 25–38. https://doi.org/10.1016/j.bandc.2015.09.004

Womelsdorf, T., Schoffelen, J.-M., Oostenveld, R., Singer, W., Desimone, R., Engel, A. K., & Fries, P. (2007). Modulation of neuronal interactions through neuronal synchronization. *Science*, *316*(5831), 1609–1612. https://doi.org/10.1126/science.1139597